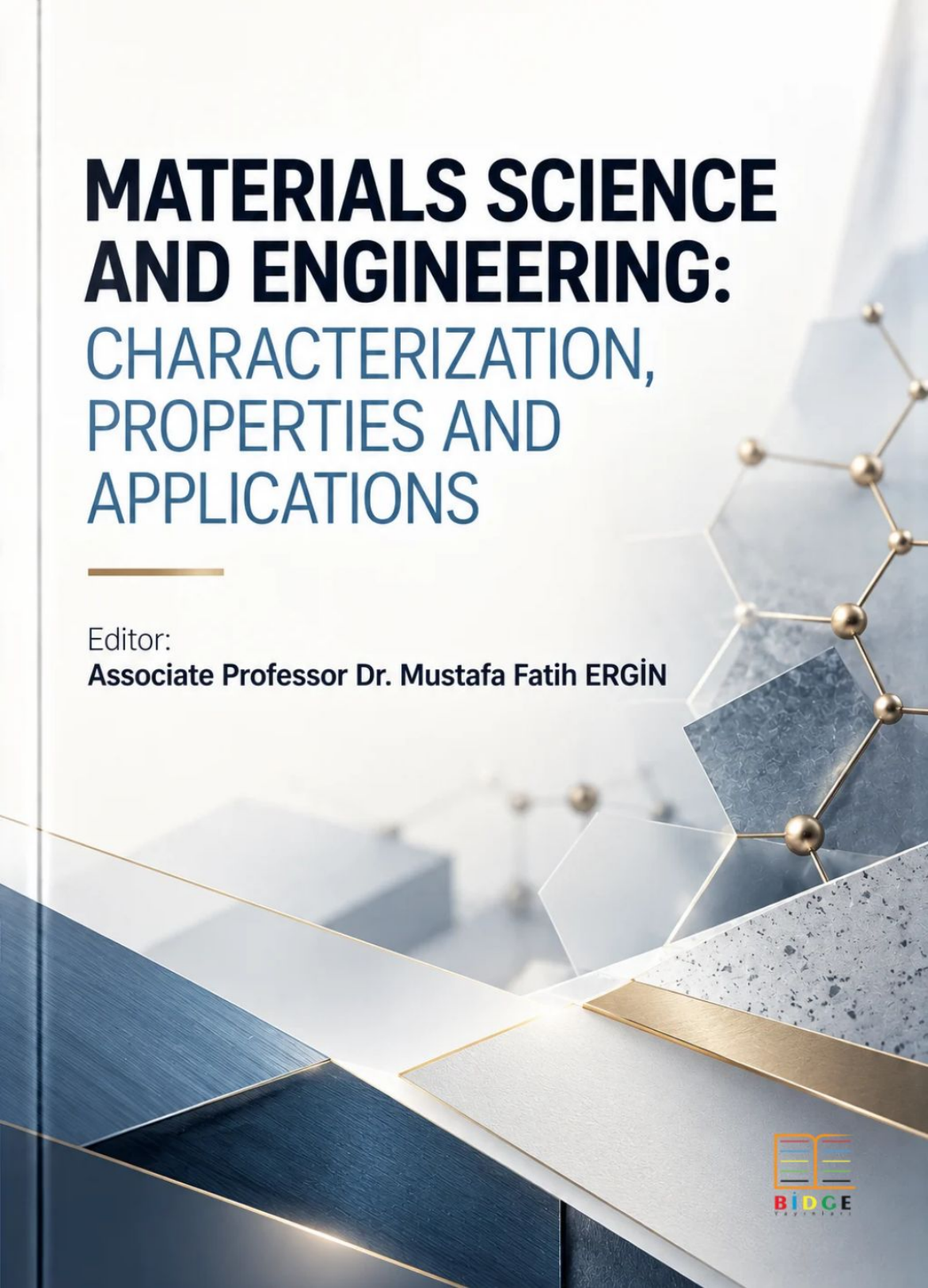
MATERIALS SCIENCE AND ENGINEERING:

CHARACTERIZATION, PROPERTIES AND APPLICATIONS

Editor:
Associate Professor Dr. Mustafa Fatih ERGİN



BİDGE Yayınları

BİDGE Yayınları

Materials Science and Engineering: Characterization, Properties And Applications

Editör: Associate Professor Dr. Mustafa Fatih ERGİN

ISBN: 978-625-5474-88-9

1. Baskı
Sayfa Düzeni: Gözde YÜCEL
Yayınlama Tarihi: 2026-10-25
BİDGE Yayınları

Bu eserin bütün hakları saklıdır. Kaynak gösterilerek tanıtım için yapılacak kısa alıntılar dışında yayıncının ve editörün yazılı izni olmaksızın hiçbir yolla çoğaltılamaz.

Sertifika No: 71374
Yayın hakları © BİDGE Yayınları
www.bidgeyayinlari.com.tr - bidgeyayinlari@gmail.com
Krc Bilişim Ticaret ve Organizasyon Ltd. Şti.
Güzeltepe Mahallesi Abidin Daver Sokak Sefer Apartmanı No: 7/9 Çankaya / Ankara

PREFACE

Understanding how materials behave during processing, application and service is central to materials science and engineering. Composition, structure, surface characteristics and environmental conditions all influence performance. Exploring the relationships among these factors provides a basis for developing useful materials, understanding their limitations and addressing practical engineering challenges. Materials Science and Engineering: Characterization, Properties and Applications brings together contributions that examine materials from complementary scientific and engineering perspectives. The book connects material preparation and characterization with the interpretation of properties and performance in practical applications. Its purpose is to show how experimental observations can inform material selection, processing decisions and the assessment of functional behaviour. Characterization provides an essential link between material preparation and an understanding of material behaviour. Considering structural, thermal, morphological and surface properties together helps researchers explore how processing choices influence function and performance. This perspective supports the interpretation of experimental findings and connects fundamental knowledge with practical engineering needs. Developing materials for practical use requires consideration of stability, durability, processing demands and resource efficiency. These interconnected factors shape both material selection and the assessment of potential applications. The contributions collected in this volume reflect the value of examining

material properties within this broader context and drawing on knowledge from different areas of science and engineering. By bringing different areas of materials research into a shared volume, this book aims to encourage readers to recognise connections across disciplinary boundaries. Concepts concerning interfaces, porosity, phase behaviour and material degradation can offer insights beyond the particular systems in which they are first studied. Sharing this knowledge can help researchers formulate new questions and approach familiar problems from different perspectives. This volume is intended for researchers, postgraduate students and professionals working in materials science, chemistry, chemical engineering and related fields. I hope that the contributions will provide a useful resource for understanding material behaviour and stimulate further investigation into the relationships between preparation, properties and practical use. I sincerely thank all contributing authors for sharing their knowledge and research. I also extend my appreciation to everyone involved in the review, preparation and publication of this volume. Their efforts have made it possible to bring these contributions together and make them available to a wider readership.

M. Fatih Ergin,

PhD Associate Professor

İÇİNDEKİLER

DEFECTS IN WATERBORNE ARCHITECTURAL PAINTS .. 1
FUNDA DEMİR

Structural and Thermal Investigation of the Phase Transition Behavior Of Ammonium Nitrate with Potassium Nitrate Addition 23
AYŞEN NUR DURGUN, İBRAHİM BULDUK

CHARACTERIZATION AND ADSORPTION APPLICATIONS OF ACTIVATED CARBONS ORIGINATING FROM RICE HUSKS 48
İLKNUR DEMİRAL, CANAN ŞAMDAN, HAKAN DEMİRAL

BÖLÜM 1

DEFECTS IN WATERBORNE ARCHITECTURAL PAINTS

FUNDA DEMİR[1]

Introduction

Architectural paints and coatings are functional surface materials applied to protect buildings and decorate them visually (Jones et al., 2017). While interior and exterior paints account for the largest share of architectural coatings, varnishes, wood stains and clear protective systems are complementary products in this category. Today, in line with sustainability principles and regulations limiting volatile organic compounds (VOCs), most of these products are waterborne latex formulations; latex-based products make up roughly three-quarters (about 77%) of the architectural segment (Jones et al., 2017). According to recent market estimates, interior paints form the backbone of the architectural coatings market with a 67% share, whereas exterior paints represent 25%. The remainder is shared among stains, varnishes, clear coatings and other products (Mitsch & Gazieva, 2024).

[1] Dr, Kalekim Construction Materials., Acrylic Coatings R&D Department, ORCID: 0000-0002-7036-434X

Solvents serve two primary purposes in paint formulations: they make it possible to manufacture the paint and to apply it to a surface (Lambourne, 1999). Although the solvent has no lasting influence on the final performance of the paint film, the solvent that remains in the film during its early life (solvent retention) can influence its hardness, flexibility and other properties (Lambourne, 1999). In the literature, the term “solvent” is also often used for liquids that do not actually dissolve the binder; such liquids are more correctly called “diluents” (Lambourne, 1999).

In waterborne systems, water dissolves some of the components but does not dissolve the main film former (binder) (Lambourne, 1999). Waterborne paints generally contain many components, including water, polymeric binders, film-forming aids (coalescents), pigments, extenders, defoamers, neutralising agents, rheology modifiers, levelling agents, preservatives, plasticizers, and wetting and dispersing agents (Arjmandi et al., 2024). Many of these ingredients are insoluble or only partly soluble in water, so the formulation tends towards instability and phase separation. Amphiphilic (both water- and oil-loving) components are added to counter this; however, they create complex interactions among the components, which makes the final film properties harder to control (Arjmandi et al., 2024).

This complexity of the formulation, the interactions between components and variations in drying conditions can lead to various coating defects. Coating defects are generally examined in three main categories (Fitzsimons & Parry, 2010):

- **Defects occurring during application:** These mainly arise from rheological properties and surface tension differences (Lambourne, 1999). Examples: sagging and cissing.

- **Defects occurring after application, before entering service:** These develop during film formation and drying. Examples: blushing and wrinkling.
- **Defects occurring during service:** These develop over time as the coating is exposed to outdoor conditions. Example: chalking (Fitzsimons & Parry, 2010).

In the following sections, defects that develop inside the container during storage are also addressed as a separate group, in addition to these three categories.

Defects Observed in Waterborne Architectural Paints

Fitzsimons and Parry (2010) classify coating defects into three groups: those arising during application, those that develop after application but before the coating enters service, and those appearing in service. Because waterborne paints can also deteriorate before they are used, this chapter adds storage as a fourth stage. The main defects of waterborne architectural paints are therefore discussed in four groups that follow the life cycle of the paint. For each defect, the definition is given first, followed by the mechanism of formation and, finally, the formulation and application measures used to prevent it.

Defects Occurring During Storage

The quality and performance of a waterborne paint depend on the formulation remaining stable throughout its shelf life. In-can defects arise when the paint fails to maintain its colloidal or microbiological stability during storage, and they become visible in the container before the paint is applied. Typical examples include pigment settling and skin formation inside the can (Lambourne, 1999). Latex paints are also highly susceptible to microbial spoilage (Jeffs & Jones, 1999). The main defects encountered during storage are explained below.

Settling and Hard Settling

Pigments and extenders generally have a higher density than the liquid phase and binder of the paint and therefore, they tend to settle under the influence of gravity. This physical process is fundamentally expressed by Stokes' law (Doroszkowski, 1999):

$$d = (18\eta h / \Delta\rho g t)^{1/2} \quad (1)$$

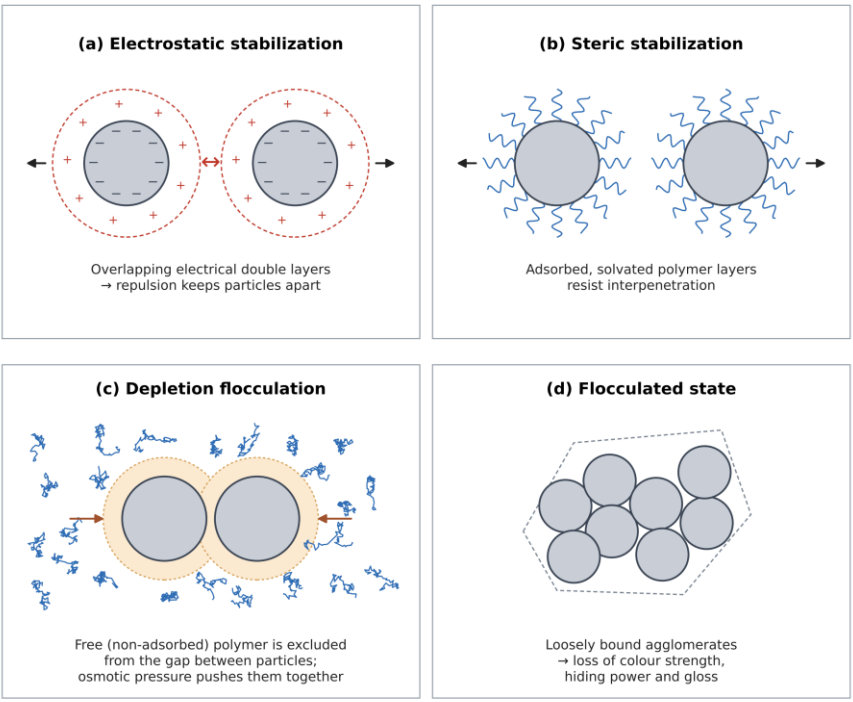
where d is the particle diameter (Stokes diameter), η the viscosity of the medium, h the settling distance, Δρ the density difference between the particle and the medium, g the gravitational acceleration, and t the time.

Settling in the can is the accumulation of pigment and filler particles at the bottom of the container due to gravity during storage. When the particles pack tightly into a compact layer that cannot be redispersed by simple stirring, it is referred to as hard settling. Settling arises because the viscosity of the paint at the very low shear rates prevailing during storage is insufficient to keep the particles suspended. However, raising this low-shear viscosity to improve storage stability can impair levelling during application; a balance must therefore be struck between settling, sagging and brushmark levelling (Graystone, 1999). Notably, well-deflocculated dispersions, which favour gloss and opacity, tend to sediment into a hard, compact deposit that is difficult to redisperse, whereas a degree of controlled structure in the paint resists settlement (Doroszkowski, 1999; Jeffs & Jones, 1999). In latex paints, such a rheological structure is usually built into the formulation, so settling is generally less of a problem than in solvent-based paints (Jeffs & Jones, 1999). Settling is therefore controlled mainly through the choice of thickeners and anti-settling additives rather than by maximising pigment dispersion.

Flocculation (Agglomeration)

Flocculation is the formation of loosely bound pigment agglomerates within the paint (Fitzsimons & Parry, 2010). In waterborne paint systems, particles are generally kept stable through electrostatic and steric mechanisms (Bentley, 1999). However, free polymer dissolved in the aqueous phase and not adsorbed onto the particle surface can induce agglomeration through an osmotic (entropic) mechanism known as depletion flocculation (Figure 1) (Doroszkowski, 1999). In latex paints, this may occur simply on the addition of an otherwise inert thickening agent (Doroszkowski, 1999). Flocculation is primarily caused by non-uniform pigment dispersion, which may result from the use of inappropriate thinners, insufficient mixing or incorrect surfactant selection (Fitzsimons & Parry, 2010). The defect reduces colour strength and colour consistency, hiding power and gloss (Abel, 1999; Jeffs & Jones, 1999). Proper selection and dosage of dispersants, along with verifying the compatibility of colorants with the system, play a decisive role in preventing this issue.

Figure 1. Schematic representation of (a) electrostatic and (b) steric stabilization of pigment particles, (c) depletion flocculation induced by non-adsorbed free polymer, and (d) the resulting flocculated state.



Source: Prepared by the author with the assistance of an AI tool (Claude, Anthropic) using Python/Matplotlib, based on Bentley (1999) and Doroszkowski (1999).

Microbial Degradation and Viscosity Loss

Latex-based and other waterborne paints are particularly susceptible to microbial spoilage. Bacterial contamination can lead to gas formation inside the container, while enzymatic degradation of cellulosic thickeners causes a loss of viscosity (Jeffs & Jones, 1999). This susceptibility is not unique to the finished product; polymer dispersions used as raw materials are also prone to

microbial contamination (Müller et al., 2020). Good hygiene practices during production serve as a primary preventive measure; however, in-can preservatives remain necessary to ensure the required shelf life (Jeffs & Jones, 1999). The use of such in-can preservatives effectively prevents microbial degradation of the paint during storage.

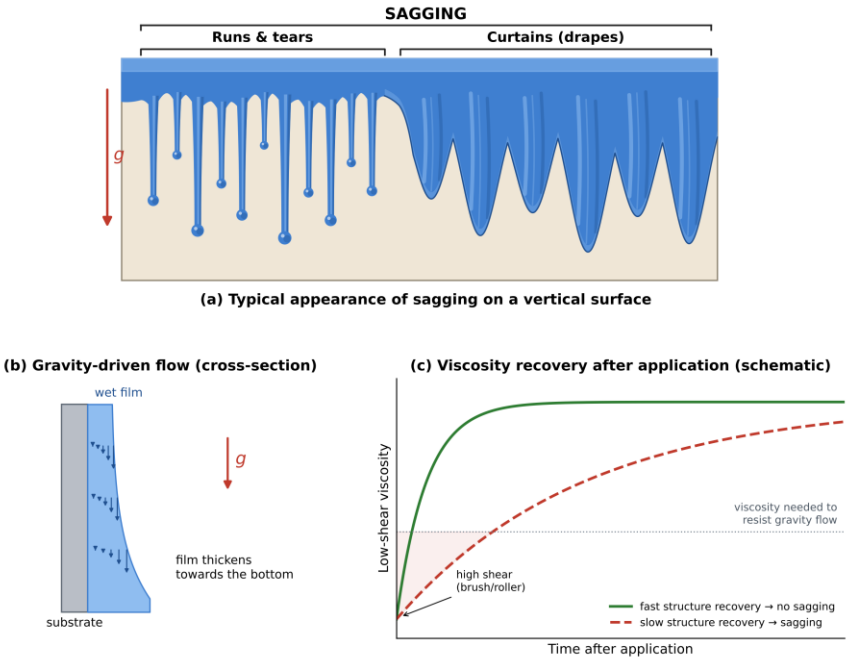
Defects Occurring During Application

Defects in this group occur during and immediately after the application of the paint by brush, roller, or spray, while the film is still fluid. These defects are mainly associated with the rheology and surface chemistry of the paint (Lambourne, 1999). In decorative paints, avoiding defects such as sagging (dripping), brush marks, and roller spatter while maintaining good application properties requires finely tuned rheological properties (Graystone, 1999).

Sagging

Sagging is the formation of an irregular coating resulting from the excessive flow of paint applied to vertical surfaces (Figure 2) (Lambourne, 1999). The defect appears shortly after application in the form of runs or tears, and in severe cases, as curtains. Its most common causes are excessive film thickness and the excessive addition of thinner (Fitzsimons & Parry, 2010). Solution-based systems, owing to their better flow, are more prone to sagging and runs on vertical surfaces than dispersion-based paints (Graystone, 1999). Preventing sagging depends on the rapid recovery of structure (low-shear viscosity) after application, achieved, for example, with thixotropic or anti-sag additives, and on keeping the film thickness under control (Jeffs & Jones, 1999).

Figure 2. Sagging of a wet paint film: (a) typical appearance on a vertical surface as runs/tears and curtains; (b) gravity-driven downward flow, leading to a film that thickens towards the bottom; (c) schematic of low-shear viscosity recovery after application — paints whose structure recovers quickly resist gravity flow, whereas slow recovery leads to sagging.



Source: Prepared by the author with the assistance of an AI tool (Claude, Anthropic) using Python/Matplotlib, based on Fitzsimons and Parry (2010) and Strivens (1999).

Cissing (Crawling)

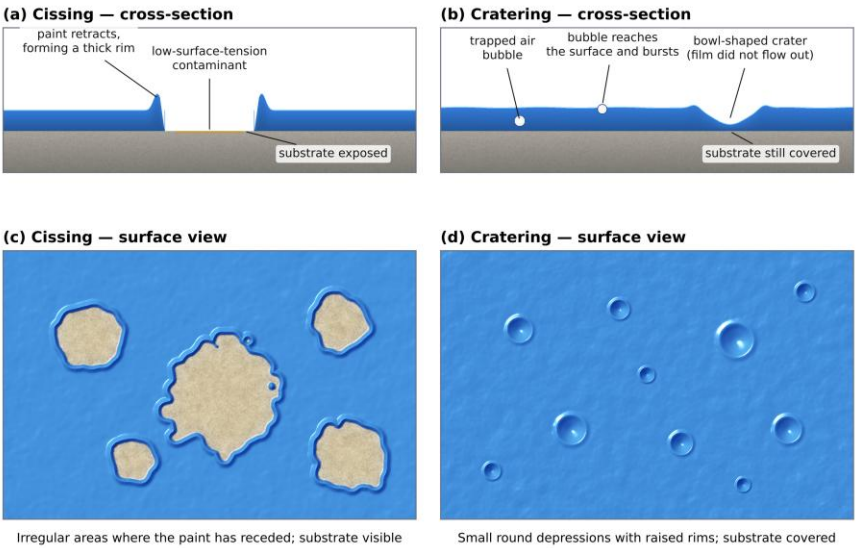
Cissing is a surface defect occurring when a wet paint film fails to adequately wet the substrate, thereby receding and exposing the underlying surface; the affected areas can range from localized recessions to quite broad exposed patches (Fitzsimons & Parry, 2010). The defect is caused by a localized change in the surface tension of the film (Lambourne, 1999).

The primary drivers of this defect include low-surface-energy contaminants on the substrate such as oil, grease or silicone—as well as improper solvent blends (Fitzsimons & Parry, 2010). Additionally, the misapplication of additives can induce this issue. For instance, a surfactant added to improve wetting may generate foam; the silicone defoamer subsequently incorporated to suppress the foam causes cissing, which is then counteracted by adding further surfactant. Jeffs and Jones (1999) term this repetitive cycle "spiral formulation". To prevent cissing, the substrate must be thoroughly cleaned and degreased, and silicone-based additives must be selected and dosed carefully.

Cratering

Cratering is a surface defect in which small, bowl-shaped depressions form in the paint film. Although it may look similar to cissing, the two defects should be distinguished (Figure 3): in cissing, the paint recedes and exposes the substrate, whereas a crater is a depression within the film itself. Cratering is typically caused by air bubbles trapped in the wet film, which burst as the coating dries; if the paint does not have enough time to flow out before it sets, these bursts remain as small craters in the dried film (Fitzsimons & Parry, 2010). Prevention therefore relies on minimizing air entrainment during mixing and application.

Figure 3. Comparison of cissing and cratering. (a) Cissing in cross-section: the wet paint retracts from a low-surface-tension contaminant, forming a thickened rim and exposing the substrate. (b) Cratering in cross-section: a trapped air bubble rises and bursts during drying, leaving a bowl-shaped depression while the substrate remains covered. (c, d) Typical surface appearance of each defect.



Source: Prepared by the author with the assistance of an AI tool (Claude, Anthropic) using Python/Matplotlib, based on Fitzsimons and Parry (2010) and Lambourne (1999).

Brush Marks (Poor Levelling)

Brush marks are ridges and furrows left in the dried film when the applied paint does not flow out sufficiently after brushing (Fitzsimons & Parry, 2010). In dispersion-based paints, the likelihood of such irregularities persisting in the film is higher compared to solution-based coatings; this particularly impairs the appearance of higher-gloss systems (Graystone, 1999). In the paints studied by Strivens (1999), thixotropic structure recovery appeared

to have a stronger influence than solvent loss on the initial stages of brushmark flow-out. To prevent this defect, rheology modifiers that allow the structural recovery to be controlled, such as associative thickeners, should be selected (Graystone, 1999), and the paint should have a sufficient open time.

Foam and Pinholes

Pinholes occur when air or gas bubbles present in a wet film burst during application or drying, leaving behind minute holes that fail to close before the film dries (Fitzsimons & Parry, 2010). They are also a common problem on porous substrates, from which air can be released into the wet film (Fitzsimons & Parry, 2010). In water-based paints, surfactants added to improve wetting can stabilize these bubbles and promote foaming; however, the excessive or improper use of silicone defoamers to suppress the foam can lead to new defects such as cissing (Jeffs & Jones, 1999). Drying conditions are also a critical factor; for instance, the rapid evaporation of water at high temperatures can result in defects like pinholes and bubbles (Arjmandi et al., 2024). To prevent these issues, the type and dosage of the defoamer should be optimized, and both the application technique and environmental conditions must be carefully controlled.

Lapping Marks and Wet Edge

The time interval preceding the onset of drying at the edges of a latex film is referred to by industrial scientists as the “lapping time”, whereas in the scientific literature the time at which water recedes from the film edge is often called the “open time” (Keddie & Routh, 2010). When painting large continuous surfaces, such as walls, if the work is interrupted before the adjacent section is completed, a visible boundary mark often forms at the junction of the two applied regions (Keddie & Routh, 2010). This phenomenon stems from the non-homogeneous drying of latex films, in which a

drying front advances progressively from the film edge inward (Keddie & Routh, 2010). In matt paints, the consequences of lapping are not readily visible and have generally been tolerated, whereas in mid-sheen paints such flow deficiencies become more visible (Graystone, 1999). To mitigate this defect, the open time of the paint should be extended through formulation, and application should proceed continuously so that a wet edge is maintained.

Defects Arising After Application and Before Service

The defects in this group arise during the formation and drying of the paint film. Latex film formation is generally described in three stages: (I) evaporation of water and regular arrangement of particles, (II) deformation of particles, (III) diffusion of polymer chains along particle boundaries (Keddie, 1997).

By most definitions, stage II cannot take place below the minimum film-forming temperature (MFFT), and stage III cannot take place below the glass transition temperature (Tg) of the polymer (Keddie, 1997). Although these stages proceed sequentially in any given region of the film, different regions of the same film may be at different stages at the same time (Keddie & Routh, 2010). Most of the defects discussed in this section can be related to a disturbance in one of these stages. Wrinkling, which was mentioned as an example in the introduction, is characteristic mainly of solvent-borne systems and is therefore not discussed separately here.

Poor Film Formation at Low Temperature

When a paint is applied at a temperature below its MFFT, the polymer particles cannot coalesce sufficiently, and a continuous film fails to form (Keddie, 1997). Low temperatures hinder both the coalescence of the particles and the evaporation of water, resulting in a weak and porous coating (Arjmandi et al., 2024). In standard test methods, the MFFT is defined as the lowest temperature at which film formation occurs (Keddie, 1997). Latex particles with a Tg

above the ambient temperature cannot form a film on their own (Arjmandi et al., 2024); therefore, film-forming additives, known as coalescing agents, are incorporated into the formulation. These substances facilitate film formation by temporarily softening the polymer (Arjmandi et al., 2024). To prevent inadequate film formation, the MFFT of the product should be adjusted to suit the expected application conditions, and application at low temperatures should be avoided.

Skinning (Crust Formation)

During the drying of latex films, when the rate of water evaporation exceeds the diffusion rate of the polymer particles within the film, corresponding to a high Péclet number (Pe $\gg$ 1), particles preferentially accumulate at the top surface of the film. The coalescence of these surface-concentrated particles into a continuous polymer skin acts as a barrier to further water evaporation, thereby substantially prolonging drying (Figure 4a) (Keddie & Routh, 2010). Skinning is therefore commonly observed when thicker films are applied (Keddie & Routh, 2010).

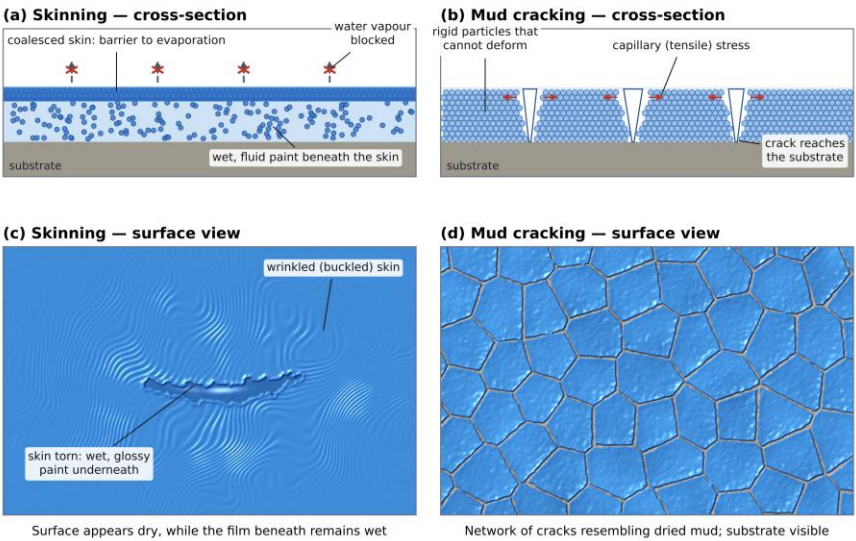
The underlying physics hinges on particle mobility: strong particle diffusion maintains a uniform concentration profile throughout the film thickness, whereas weak diffusion leads to surface accumulation and skin formation (Routh, 2013). A modelling study reviewed by Arjmandi et al. (2024) showed that, at constant film thickness and drying conditions, a lower polymer Tg promotes skinning and extends the drying time. The same study found that skin formation can be reduced by applying thinner films, by increasing the evaporation rate in the early stage of drying, or by using a polymer of higher viscosity.

Mud Cracking

Mud cracking is a surface defect characterized by a dried paint film covered with a network of cracks of varying sizes,

resembling a dried-out mud surface. This defect is particularly associated with the over-application of heavily pigmented or water-based coatings (Fitzsimons & Parry, 2010). During drying, the flow of water through the packed particle layer generates a pressure drop and capillary pressure. When the particles are not deformable enough to accommodate this stress, the film cracks (Figure 4b) (Keddie & Routh, 2010). It is now widely accepted that capillary pressure is the driving force behind this cracking (Keddie & Routh, 2010). Films below a certain thickness do not crack; this threshold is known as the critical cracking thickness (Routh, 2013). The drying rate also plays a role: as the drying rate increases, latex films may first craze and, at the highest rates, crack (Steward et al., 2000). To prevent mud cracking, the applied film thickness should be limited, the particles should be made sufficiently deformable during film formation, for example by using an adequate level of coalescing agent (Arjmandi et al., 2024), and excessively fast drying should be avoided.

Figure 4. Comparison of skinning and mud cracking. (a) Skinning: particles accumulate and coalesce at the top surface, forming a skin that acts as a barrier to further evaporation while the paint beneath remains wet. (b) Mud cracking: capillary (tensile) stress in a packed layer of particles that cannot deform causes cracks that extend to the substrate. (c) A skinned surface may wrinkle, and where the skin is broken, wet paint is exposed. (d) Typical mud-crack network.



Source: Prepared by the author with the assistance of an AI tool (Claude, Anthropic) using Python/Matplotlib, based on Keddie and Routh (2010), Routh (2013), and Fitzsimons and Parry (2010).

Surfactant Exudation and Water Spotting

Surfactants used during latex synthesis and paint formulation can remain mobile even after film formation (Keddie & Routh, 2010). The migration of surfactants toward an interface is termed “exudation” (Keddie & Routh, 2010). Surfactant accumulation on the film surface is undesirable, as it has adverse effects on appearance, wetting and adhesion (Palmer et al., 2022). Tacky surfactant layers have also been linked to increased dirt pick-up and

mould growth (Keddie & Routh, 2010). Water spotting appears as marks left on the film where drops of water, such as rain or dew, have dried on the surface. Drops falling on wet paint can leave permanent marks, whereas marks on a freshly dried film can often be rubbed off (Fitzsimons & Parry, 2010). In latex paints, such marks are commonly attributed to water-soluble components, such as surfactants, that are drawn to the surface of a fresh film and left behind when the water evaporates. To prevent these defects, surfactant levels should be kept low, since exudation becomes significant mainly at concentrations above surface coverage (Steward et al., 2000). Reactive (polymerisable) surfactants can also be used: they are chemically bound to the polymer and therefore cannot desorb or exude (Keddie & Routh, 2010). Finally, good particle coalescence should be ensured, because fully coalesced films carry far less surfactant at their surface than films in which the particles are only partly deformed (Palmer et al., 2022).

Blushing (Water Whitening)

Blushing appears as a hazy, dull surface that forms when the film is exposed to moisture before it has fully cured (Fitzsimons & Parry, 2010); in latex films, it is often called water whitening. Surfactant accumulated at the particle boundaries may form hydrophilic pathways for water (Keddie & Routh, 2010), and water trapped in small pockets scatters light because its refractive index differs from that of the polymer, making the film look hazy or cloudy (Keddie & Routh, 2010). Waterborne coatings generally absorb more water than solvent-based coatings (Arjmandi et al., 2024), so the risk is greatest when the film meets moisture before coalescence is complete (Steward et al., 2000). To prevent this defect, free surfactant content should be kept low, adequate drying time should be allowed, and application under high humidity or condensation should be avoided (Fitzsimons & Parry, 2010).

Defects Arising During Service

The defects in this group appear after the paint has entered service (Fitzsimons & Parry, 2010). They develop gradually under the long-term action of UV radiation, moisture, temperature changes, the chemistry of the substrate and biological agents. Water is involved in most of these processes. For example, wood is subject to biodegradation and moisture movement, and concrete is a highly alkaline surface. Controlling processes in which water takes part can therefore be regarded as one of the main functions of a paint film (Graystone, 1999).

Blistering, Flaking, and Delamination

Flaking describes paint coming away from the substrate, whereas delamination denotes intercoat separation in a multicoat system; both are forms of adhesion failure (Fitzsimons & Parry, 2010). Blistering is characterised by dome-shaped elevations in the dry film resulting from localised loss of adhesion (Fitzsimons & Parry, 2010). Osmotic blistering is commonly associated with soluble salts, soluble pigments or retained solvents in the film (Fitzsimons & Parry, 2010). Blistering requires a loss of adhesion and sufficient film flexibility, together with a driving force such as vapour pressure, swelling or osmotic pressure (Graystone, 1999). To prevent these defects, the substrate must be properly prepared and clean (Fitzsimons & Parry, 2010), appropriate primers must be selected (Fitzsimons & Parry, 2010), and film permeability should suit the conditions of service (Graystone, 1999).

Efflorescence

Efflorescence is a white salt deposit that forms on plaster, brickwork or the paint surface when moisture carries soluble salts from the substrate to the surface (Fitzsimons & Parry, 2010). It occurs in two forms. The bulky form usually consists of sodium sulphate and can disrupt paint films of low permeability. The denser

form is usually calcium carbonate, also known as lime bloom; it is harder to remove but can be painted over after light abrasion (Graystone, 1999). Heavy salt deposits, however, can still cause adhesion failure, so painting should be postponed until efflorescence has largely stopped (Graystone, 1999).

Chalking

Chalking appears as a loose, powdery layer on the paint surface, often together with colour change or fading. It results from the breakdown of the binder under weathering and UV light, which leaves pigment particles at the surface without enough binder to hold them in place. The rate of chalking depends on the pigment concentration and the type of binder (Fitzsimons & Parry, 2010). Titanium dioxide, particularly in its photocatalytic nano-sized form, can accelerate this breakdown. Kalinowski et al. (2025) observed significant binder decomposition in acrylic coatings containing nano-TiO_2 even under low UV-A intensities, comparable to autumn and winter sunlight in Northern and Central Europe. Chalking can therefore be limited by choosing UV-resistant binders and TiO_2 grades of low photoactivity, and by balancing photocatalytic activity against the long-term stability of the film (Kalinowski et al., 2025).

Mould Growth and Dirt Pick-Up

Under suitable conditions, most paint films can support mould growth. Biocides added to the paint can help keep the film free of such growth, but their effect is limited when the surface is heavily covered with nutrients (Jeffs & Jones, 1999). Dirt pick-up depends strongly on the binder. Harder polymers retain less dirt and resist gloss loss and scrubbing better, whereas softer polymers favour extensibility and exterior durability (Graystone, 1999). Tacky surfactant layers that accumulate at the surface have also been linked to increased dirt pick-up and mould growth (Keddie & Routh, 2010). To prevent these defects, suitable in-film biocides should be used,

binder hardness should be balanced against flexibility, and surfactant migration to the surface should be minimised.

Concluding Remarks

This chapter has examined the main defects of waterborne architectural paints by following the life cycle of the paint, from storage in the can, through application and film formation, to service on the wall. Although the defects differ in appearance, most of them can be traced to a small number of underlying causes: loss of colloidal or microbiological stability in the can, unsuitable rheology during and after application, disturbances in the stages of latex film formation, the migration of surfactants and other water-soluble species, and the action of water throughout the life of the film. Many of the preventive measures discussed also involve trade-offs. A paint must be structured enough to resist settling and sagging, yet fluid enough to level; its binder must be soft enough to form a film at the application temperature, yet hard enough to resist dirt pick-up; and its surfactants must stabilise the dispersion without later weakening the dried film. Preventing defects therefore depends less on any single additive than on a balanced formulation, applied under suitable conditions and at an appropriate film thickness.

Declaration on the Use of AI Tools

During the preparation of this chapter, the author used Claude (Anthropic) to assist with language editing, source verification and the preparation of the schematic figures.

References

Abel, A. G. (1999). Pigments for paint. In R. Lambourne & T. A. Strivens (Eds.), *Paint and surface coatings: Theory and practice* (2nd ed., pp. 91–165). Woodhead Publishing. https://doi.org/10.1533/9781855737006.91

Arjmandi, A., Bi, H., Nielsen, S. U., & Dam-Johansen, K. (2024). From wet to protective: Film formation in waterborne coatings. *ACS Applied Materials & Interfaces, 16*(43), 58006–58028. https://doi.org/10.1021/acsami.4c09729

Bentley, J. (1999). Organic film formers. In R. Lambourne & T. A. Strivens (Eds.), *Paint and surface coatings: Theory and practice* (2nd ed., pp. 19–90). Woodhead Publishing. https://doi.org/10.1533/9781855737006.19

Doroszkowski, A. (1999). The physical chemistry of dispersion. In R. Lambourne & T. A. Strivens (Eds.), *Paint and surface coatings: Theory and practice* (2nd ed., pp. 198–242). Woodhead Publishing. https://doi.org/10.1533/9781855737006.198

Fitzsimons, B., & Parry, T. (2010). Paint and coating failures and defects. (Vol. 4, pp. 2728–2745). Elsevier. https://doi.org/10.1016/B978-044452787-5.00145-1

Graystone, J. A. (1999). Coatings for buildings. In R. Lambourne & T. A. Strivens (Eds.), *Paint and surface coatings: Theory and practice* (2nd ed., pp. 330–410). Woodhead Publishing. https://doi.org/10.1533/9781855737006.330

Jeffs, R. A., & Jones, W. (1999). Additives for paint. In R. Lambourne & T. A. Strivens (Eds.), *Paint and surface coatings: Theory and practice* (2nd ed., pp. 185–197).

Woodhead Publishing. https://doi.org/10.1533/9781855737006.185

Jones, F. N., Nichols, M. E., & Pappas, S. P. (2017). *Organic coatings: Science and technology* (4th ed.). Wiley. https://doi.org/10.1002/9781119337201

Kalinowski, M., Chilmon, K., Kuziak, J., Łukowski, P., & Jackiewicz-Rek, W. (2025). Photocatalytically induced degradation of nano-TiO2-modified paint coatings under low-radiation conditions. *Coatings, 15*(3), Article 281. https://doi.org/10.3390/coatings15030281

Keddie, J. L. (1997). Film formation of latex. *Materials Science and Engineering: R: Reports, 21*(3), 101–170. https://doi.org/10.1016/S0927-796X(97)00011-9

Keddie, J. L., & Routh, A. F. (2010). *Fundamentals of latex film formation: Processes and properties*. Springer. https://doi.org/10.1007/978-90-481-2845-7

Lambourne, R. (1999). Paint composition and applications — A general introduction. In R. Lambourne & T. A. Strivens (Eds.), *Paint and surface coatings: Theory and practice* (2nd ed., pp. 1–18). Woodhead Publishing. https://doi.org/10.1533/9781855737006.1

Mitsch, F. J., & Gazieva, A. (2024). *2024 paints, coatings, adhesives: Tepid macro with bright spots*. Fermium Research. https://chemquest.com/wp-content/uploads/2024/08/2024-Paints-Coatings-Adhesives_-Tepid-Macro-with-Bright-Spots.pdf

Müller, A., Schmahl, V., & Gschrei, S. (2020). *Survey on alternatives for in-can preservatives for varnishes, paints and adhesives*. Federal Institute for Occupational Safety and

Health (BAuA). https://doi.org/10.21934/baua:report20200811

Palmer, T. R., van der Kooij, H. M., Abu Bakar, R., Duewel, M., Greiner, K., McAleese, C. D., Couture, P., Sharpe, M. K., Smith, R. W., & Keddie, J. L. (2022). How particle deformability influences the surfactant distribution in colloidal polymer films. *Langmuir, 38*(41), 12689–12701. https://doi.org/10.1021/acs.langmuir.2c02170

Routh, A. F. (2013). Drying of thin colloidal films. *Reports on Progress in Physics, 76*(4), Article 046603. https://doi.org/10.1088/0034-4885/76/4/046603

Steward, P. A., Hearn, J., & Wilkinson, M. C. (2000). An overview of polymer latex film formation and properties. *Advances in Colloid and Interface Science, 86*(3), 195–267. https://doi.org/10.1016/S0001-8686(99)00037-8

Strivens, T. A. (1999). The rheology of paints. In R. Lambourne & T. A. Strivens (Eds.), *Paint and surface coatings: Theory and practice* (2nd ed., pp. 575–597). Woodhead Publishing. https://doi.org/10.1533/9781855737006.575

BÖLÜM 2

STRUCTURAL AND THERMAL INVESTIGATION OF THE PHASE TRANSITION BEHAVIOR OF AMMONIUM NITRATE WITH POTASSIUM NITRATE ADDITIVE

AYŞEN NUR DURGUN[1]
PROF. DR. İBRAHİM BULDUK[2]

Abstract

In this study, the phase transition behavior, along with the structural, thermal, and morphological properties of samples prepared from technical-grade ammonium nitrate (TAN) and porous prilled ammonium nitrate (PPAN) modified with potassium nitrate (KNO_3), were investigated. Compositions containing 5 g and 10 g of KNO_3 were prepared based on an initial amount of 90 g of ammonium nitrate (AN). Each composition was represented by two independent preparation replicates, resulting in a total of eight samples that were characterized using X-ray diffraction (XRD), differential scanning calorimetry (DSC), thermogravimetric analysis (TGA), and scanning electron microscopy (SEM). In the DSC

1 Master's student, Afyon Kocatepe University, Chemical Engineering, ORCID: 0009-0008-5503-9988
2 Prof. Dr., Afyon Kocatepe University, Chemical Engineering, ORCID: 0000-0001-6172-7738

analyses, endothermic transition peaks were identified in the 30.19–38.75 °C range for samples containing 5.26 wt.% KNO_3 (based on total AN–KNO_3 mass), whereas no distinct peak was observed in the same temperature range for samples containing 10 wt.% KNO_3. This trend—observed in both TAN- and PPAN-based samples across both preparation replicates—indicates that a higher addition level effectively suppresses the thermal event associated with the IV↔III phase transition of AN. The XRD patterns revealed the crystalline structure of the samples, showing variations in peak positions depending on the additive level and raw material type. In the TGA analyses, the onset temperatures for the primary mass-loss step were determined to be in the range of 203.85–217.10 °C, while SEM images displayed differences in particle morphology depending on the raw material. The overall results indicate that the addition of 10% KNO_3 significantly enhances phase stabilization by suppressing phase transitions around ambient temperature, presenting a promising approach for developing phase-stabilized AN-based oxidizers.

Keywords: Phase-stabilized ammonium nitrate; Potassium nitrate; Phase stabilization; IV↔III phase transition; Thermal characterization.

Introduction

Ammonium nitrate (AN) is a crystalline oxidizing agent used in a wide range of applications—from the fertilizer industry to the formulation of civil explosives and propellants—that can exist in five distinct polymorphic crystal structures depending on the temperature. Among these polymorphs, the Phase IV (orthorhombic) ↔ Phase III (orthorhombic) transition, which occurs near ambient temperature (~32 °C), is of particular significance due to an approximately 3.6% volumetric change that takes place within the crystal lattice. In ammonium nitrate (AN) subjected to temperature

fluctuations during storage, transport, and use, these repeated phase transitions lead to particle fragmentation (crumbling), caking, a loss of mechanical strength, and increased hygroscopicity. Consequently, preventing or suppressing this thermal transition—which occurs near room temperature—is a critical requirement for the safe and stable use of ammonium nitrate.

Studies in the literature on the AN–KNO_3 binary system have shown that the addition of KNO_3 can significantly alter the solid-state phase behavior of ammonium nitrate and promote phase stability through the formation of solid solutions (Chien et al., 2005; Wu & Chan, 2008). The incorporation of potassium ions into the crystal lattice influences lattice dynamics, offering an effective method to prevent volumetric instability at ambient temperatures (Coates & Crewe, 1961; Rotariu et al., 2022). However, a comprehensive, simultaneous investigation into how industrial-grade AN raw materials—which possess distinct morphological and physical characteristics (such as technical and prilled forms)—respond to the doping process and subsequent phase stabilization remains an area in the literature that warrants further development.

The purpose of this study is to determine the effect of KNO_3 additives—applied at different concentrations (5.26% and 10% by mass)—on the phase stabilization of technical-grade ammonium nitrate (TAN) and porous prilled ammonium nitrate (PPAN), and specifically to assess the degree to which the endothermic event associated with the IV↔III phase transition is suppressed. In this study, the phase transformations of the prepared samples were monitored using differential scanning calorimetry (DSC); furthermore, their crystal structure (via XRD), thermal stability (via TGA), and particle morphology (via SEM) were comprehensively characterized to evaluate in detail the roles of the additive concentration and the type of raw material on phase behavior (Kaniewski et al., 2021; Dave & Sirach, 2023).

Materials and methods

Raw materials and experimental design

The raw materials used in the study—technical-grade ammonium nitrate (TAN) and porous prilled ammonium nitrate (PPAN)—were obtained from İGSAŞ. Potassium nitrate (KNO_3) was also sourced from İGSAŞ, and ultra-pure water was used for the preparation of the solutions. In the study, the initial amount of ammonium nitrate (AN) was kept constant at 90 g, and mixtures containing 5 g and 10 g of KNO_3 were prepared. As part of the experimental design, each composition was prepared in two independent replicates, resulting in a total of eight samples. The initial compositions and sample codes are presented in Table 1. The concentration of KNO_3 in the mixtures was calculated as a mass percentage (wt%) based on the total mass of solids (mAN + mKNO_3) (yielding 5.26 wt% and 10.00 wt%, respectively).

Table 1. Initial compositions used in the experiments and sample matching.

Experiment	AN type	AN (g)	KNO_3 (g)	KNO_3 (% by mass)
1	PPAN	90	10	10.00
2	PPAN	90	10	10.00
3	PPAN	90	5	5.26
4	PPAN	90	5	5.26
5	TAN	90	10	10.00
6	TAN	90	10	10.00
7	TAN	90	5	5.26
8	TAN	90	5	5.26

Source: Experimental data from this study.

Sample preparation

KNO_3-doped samples were prepared via the co-crystallization of AN and KNO_3 salts in an aqueous medium. 10 mL of pure water was added to the salt mixtures (prepared in specific proportions), and the mixture was heated to 200 °C while being stirred with a magnetic stirrer for 20 minutes until a homogeneous solution was obtained. Once fully dissolved, the mixture was left to cool in a controlled manner to room temperature. The resulting crystalline products were dried in an oven at 50 °C for 72 hours to ensure the complete removal of moisture. The dried products were then ground in a mortar to achieve a homogeneous particle size distribution and stored in a desiccator to prevent moisture absorption until the analysis phase. Throughout all laboratory procedures, the utmost care was taken to adhere to safety protocols for the handling of AN (U.S. Environmental Protection Agency et al., 2015).

Characterization conditions

The crystal structures of the samples were examined using an X-ray diffractometer (XRD) with Cu-Kα radiation (λ = 1.5406 Å). The measurements were conducted at 40 kV and 40 mA, over a 2θ range of 5°–90°, with a step size of 0.02°.

Phase transitions and thermal behaviors were determined using a differential scanning calorimetry (DSC) instrument. The analyses were conducted in a helium atmosphere (flow rate of 25 mL/min) using hermetic aluminum crucibles, over a temperature range of -55 °C to +120 °C, at a heating rate of 10 °C/min, and without any isothermal holding steps.

Thermogravimetric analyses (TGA) were conducted in a nitrogen atmosphere (90 mL/min) over a temperature range of 25–900 °C, using a heating rate of 10 °C/min.

The surface and particle morphologies of the samples were examined using scanning electron microscopy (SEM) at various magnifications and an accelerating voltage of 15 kV.

Findings and discussion

Evaluation of crystal structure and XRD patterns

An examination of the XRD diffraction patterns for all samples revealed the presence of sharp, high-intensity peaks, indicating a high degree of crystallinity (Figure 1). The primary diffraction peaks are concentrated in the 2θ ranges of approximately 26°–28° and 34°, which is consistent with the AN Phase IV structure reported in the literature. The precise 2θ positions corresponding to these three distinct peak regions are listed in Table 2.

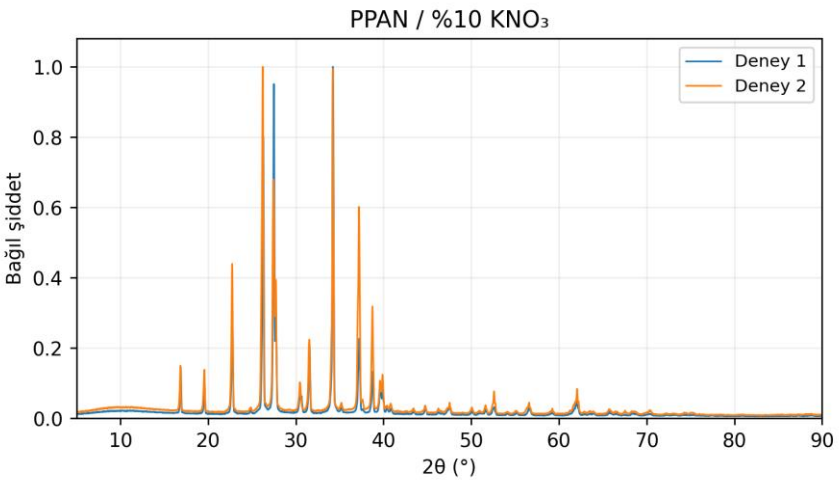
Table 2. 2θ positions of the local maxima in the three distinct peak regions. The values were read from patterns with a data interval of approximately 0.02°.

Experiment	Peak region 1 (°)	Peak region 2 (°)	Peak region 3 (°)
1	26.28	27.50	34.22
2	26.24	27.46	34.22
3	26.18	27.38	34.14
4	26.38	27.58	34.32
5	26.32	27.56	34.30
6	26.24	27.48	34.22
7	26.28	27.50	34.24
8	26.56	27.84	34.46

Source: Experimental data from this study.

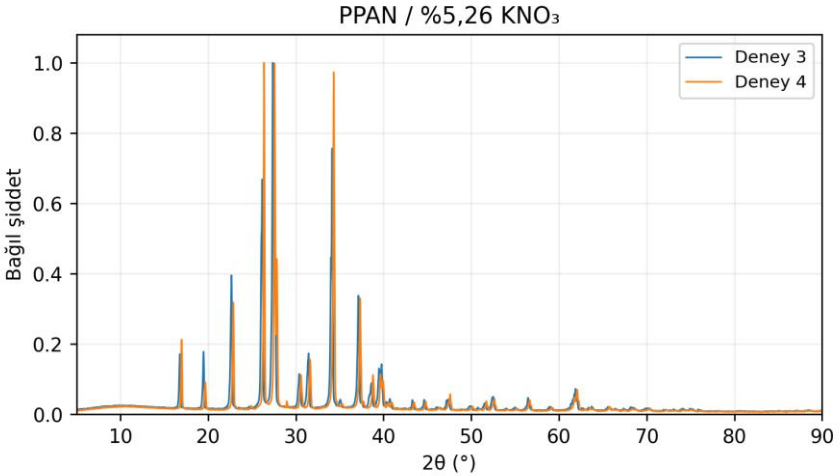
Small shifts in peak angles, ranging from 0.1° to 0.3°, were observed, depending on the doping level and the type of raw material. These shifts can be explained by the formation of a solid solution and the resulting micro-contractions in the crystal lattice—a consequence of K^+ cations (with an ionic radius of 138 pm) replacing NH_4^+ cations (with a radius of 148 pm) within the lattice (isomorphic substitution) (Coates & Crewe, 1961). The absence of any prominent, independent secondary peaks corresponding to a separate, dissociated KNO_3 phase in the diffraction patterns indicates that the co-crystallization process successfully facilitated the formation of a solid solution.

Figure 1(a). XRD patterns of PPAN / 10% KNO_3.



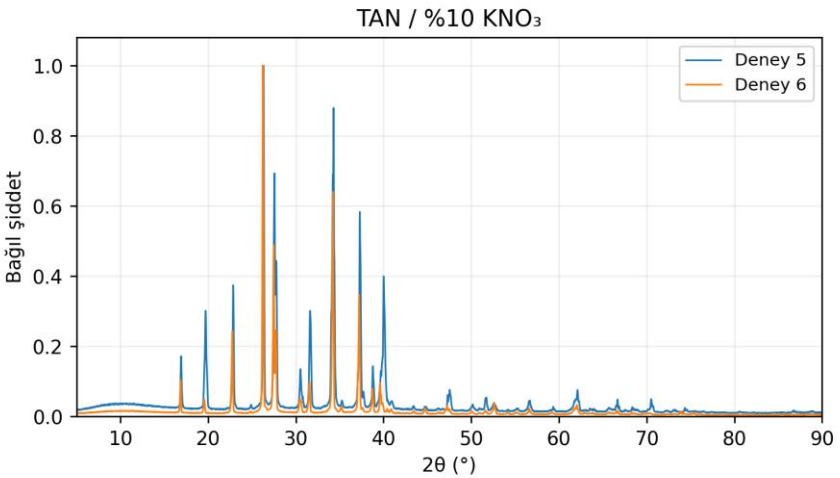
Source: Experimental data from this study.

Figure 1(b). XRD patterns of PPAN / 5.26% KNO_3.



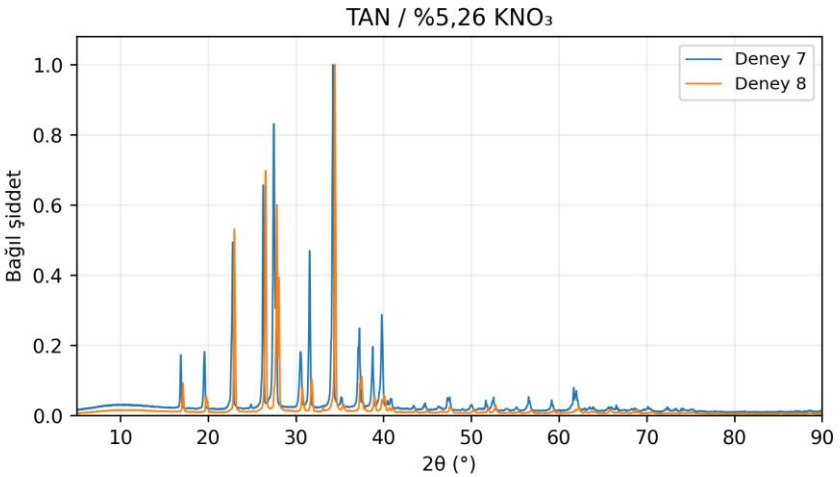
Source: Experimental data from this study.

Figure 1(c). XRD patterns of TAN / 10% KNO_3.



Source: Experimental data from this study.

Figure 1(d). XRD patterns of TAN / 5.26% KNO_3.



Source: Experimental data from this study.

Caption for Figure 1: XRD patterns of eight samples, compared using two preparation replicates for each. Each pattern is normalized to its own maximum. The curves are plotted from numerical 2θ–intensity data.

Variations in peak positions and relative intensities, dependent on the doping level and the type of raw material, have been observed in the XRD patterns. These changes reflect the influence of the KNO_3 dopant on the crystalline environment and provide structural support for the phase transition behavior—as a function of dopant concentration—that was determined via DSC. The formation of a solid solution, as reported for the AN–KNO_3 system, offers a mechanism consistent with these observed structural changes (Coates & Crewe, 1961).

Evaluation of DSC transitions based on their contribution ratio

The primary finding from the DSC results is the absence of a transition peak near ambient temperature in samples containing 10% KNO_3 (Table 3 and Figure 2). While no distinct endothermic peak is

observed in this region for experiments 1, 2, 5, and 6, peaks appear in the 30.19–38.75 °C range for experiments 3, 4, 7, and 8, which contain 5.26% KNO_3. The observation of this same trend in both PPAN and TAN samples, across two separate preparation replicates, indicates that the addition of 10% KNO_3 effectively and reproducibly suppresses the thermal event associated with the IV↔III transition.

Table 3. Summary of transition signals in the DSC thermograms, by experiment. "Not detected" indicates that no distinct peak was observed in the relevant temperature region.

Experiment	KNO_3 (%)	Ambient zone peak (°C)	ΔH (J/g)	High-temperature threshold (°C)
1	10.00	Not distinguished	—	114.84
2	10.00	Not distinguished	—	114.56
3	5.26	34.00	6.988	104.01
4	5.26	38.75	2.310	104.37
5	10.00	Not distinguished	—	114.00
6	10.00	Not distinguished	—	116.07
7	5.26	30.19	8.057	104.95
8	5.26	30.47	8.994	104.62

Source: Experimental data from this study.

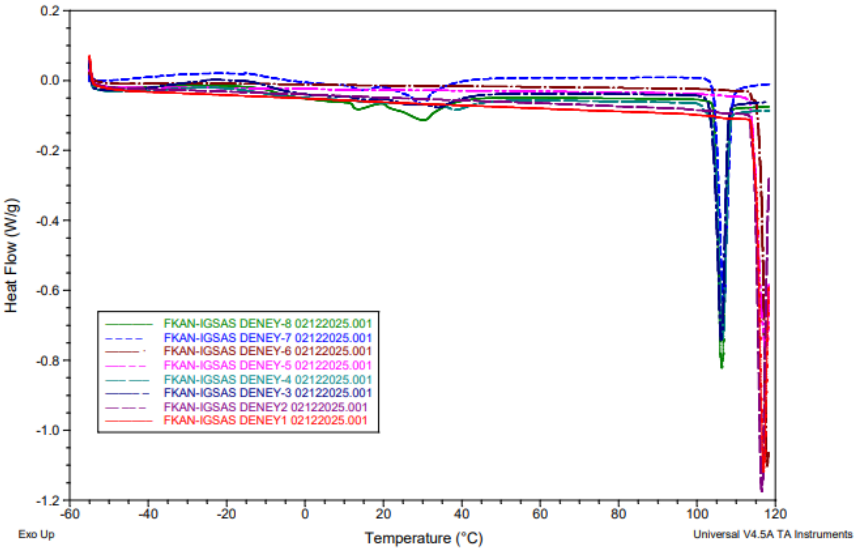
The ΔH values associated with the transitions observed in samples with low additive content fall within the range of 2.310–8.994 J/g. In contrast, the absence of a distinct transition peak in the

same temperature region for the four samples containing 10% KNO_3 clearly demonstrates the influence of the additive level on phase transition behavior.

In samples containing 10% KNO_3, the onset temperatures for endothermic events at high temperatures are recorded at approximately 114–116 °C, while for samples containing 5.26% KNO_3, they are approximately 104–105 °C. This difference indicates that the KNO_3 content influences the thermal behavior of AN not only around ambient temperature but also during solid-state events occurring at higher temperatures.

In the literature, the phase regions and transition pathways in the AN–KNO_3 system as a function of the KNO_3 proportion have been reported (Chien et al., 2005; Wu & Chan, 2008). Consistent with these studies, the current DSC results indicate that the addition of 10% KNO_3 significantly modifies the phase transition behavior around ambient temperature.

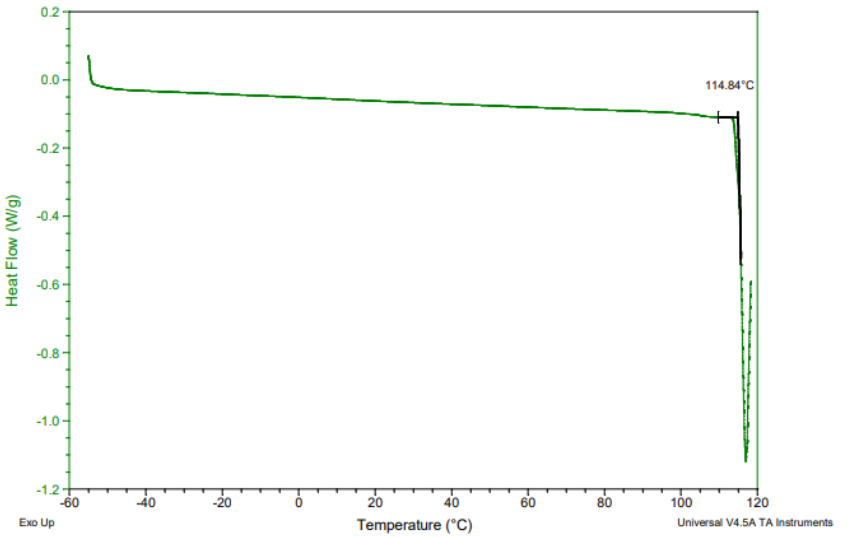
Figure 2. DSC comparison plot of eight KNO_3-doped samples. Sample numbers are provided in the legend; the exothermic direction is upward.



Source: Experimental data from this study.

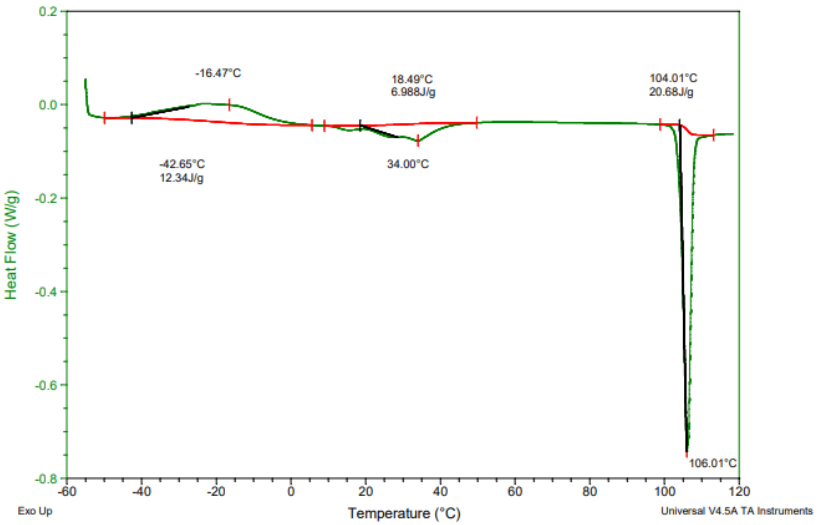
Representative DSC curves

Figure 3(a). DSC curve of the Experiment 1 / PPAN / 10% sample.



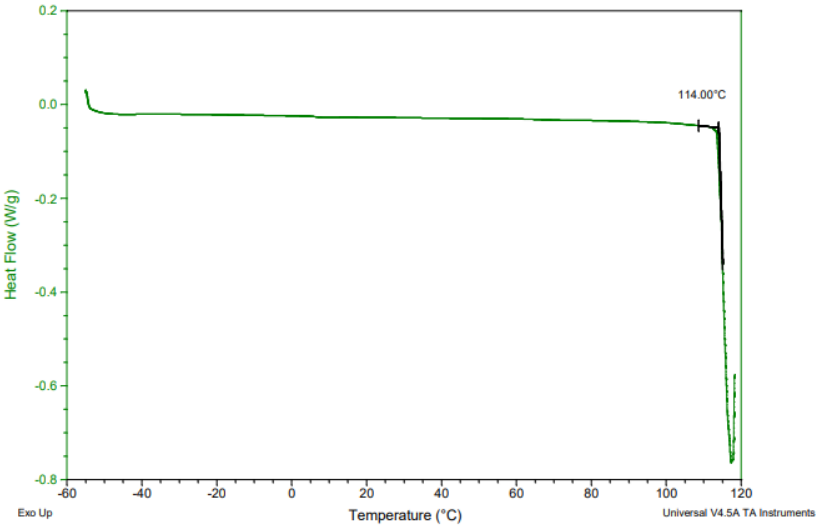
Source: Experimental data from this study.

Figure 3(b). DSC curve of the Experiment 3 / PPAN / 5.26% sample.



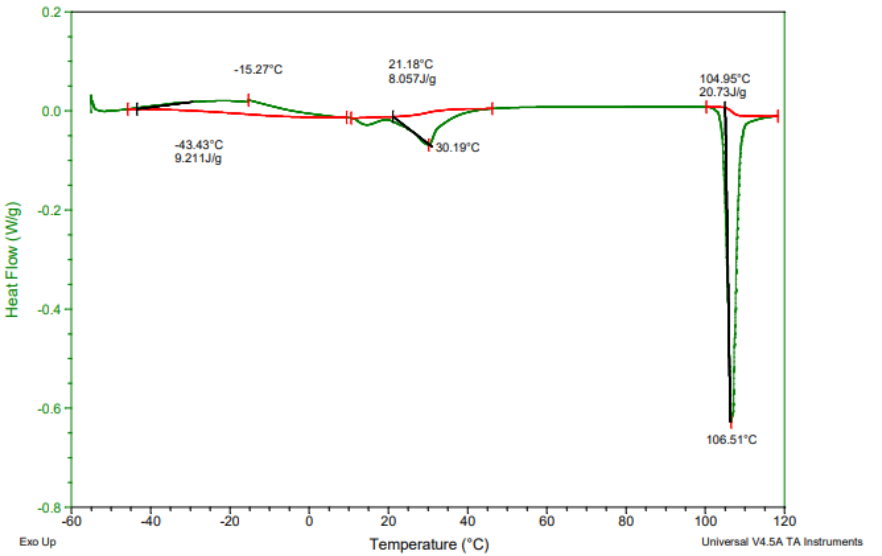
Source: Experimental data from this study.

Figure 3(c). DSC curve of the Experiment 5 / TAN / 10% sample



Source: Experimental data from this study.

Figure 3(d). DSC curve of the Experiment 7 / TAN / 5.26% sample.



Source: Experimental data from this study.

Description for Figure 3: DSC curves for Experiments 1, 3, 5, and 7, representing four compositions. The original plots and integration markers have been preserved. The curves were evaluated by considering temperature, heat flow, and the corresponding integration values together for each panel.

TGA mass loss behavior

A distinct, primary mass-loss step was observed for the eight samples in the TGA curves (Figure 4). The onset temperatures for this primary mass loss were determined to be in the range of 203.85–217.10 °C, and these values are presented in Table 4. The TGA results provide complementary insight into the thermal behavior of the KNO_3-doped samples at high temperatures.

Table 4. Onset temperatures marked for the main mass loss step in the TGA curves.

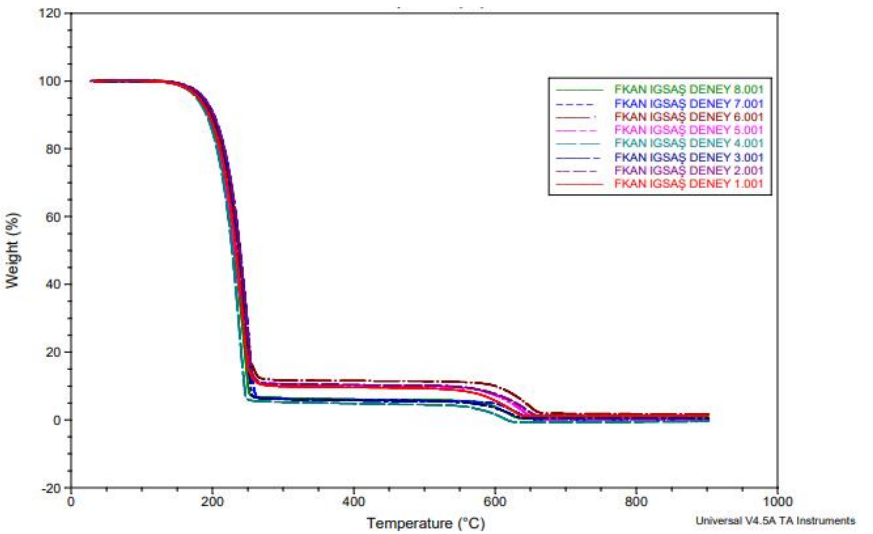
Experiment	AN type	KNO_3 (%)	Marked start (°C)
1	PPAN	10.00	209.78
2	PPAN	10.00	216.70
3	PPAN	5.26	214.74
4	PPAN	5.26	206.44
5	TAN	10.00	203.85
6	TAN	10.00	213.81
7	TAN	5.26	217.10
8	TAN	5.26	208.75

Source: Experimental data from this study.

The primary mass loss begins in the range of 203.85–217.10 °C, representing the thermal dissociation and decomposition

reactions of ammonium nitrate (AN). While pure AN completely converts into gaseous products and evaporates at approximately 260–300 °C, the TGA curves exhibit a horizontal plateau above 260 °C. This residual mass, observed between approximately 260 °C and 600 °C, corresponds to the non-volatile KNO_3 component. Indeed, the mass residue on this plateau is approximately 10% for the series with 10% doping, and approximately 5% for the series with 5.26% doping. A second, minor mass loss observed above 600 °C reflects the thermal decomposition of KNO_3 into potassium nitrite and oxide structures. These residue profiles confirm that the targeted stoichiometric doping ratios are fully maintained in the samples following synthesis.

Figure 4. TGA comparison plot for samples from Experiments 1–8. The curves show the main mass-loss step and the residual profiles at high temperatures.



Source: Experimental data from this study.

The TGA curves also show the residue profiles at high temperatures following the main mass-loss step. Studies reporting similar thermal behavior in AN systems containing potassium salts

provide literature support for the evaluation of the current results (Rotariu et al., 2022).

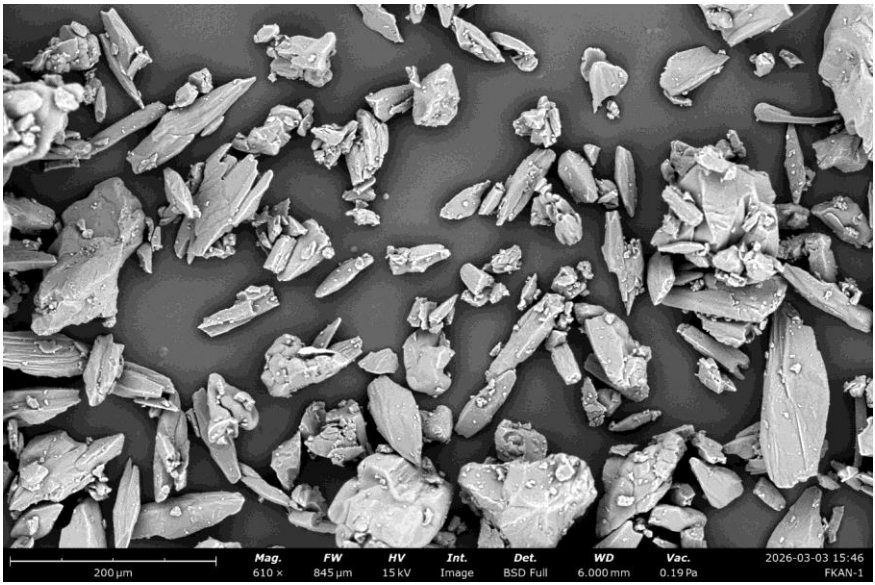
Examination of particle morphology using SEM

Electron microscope images of the synthesized products (Figure 5) revealed that the source of the raw material has a significant directing effect on the final microstructure.

In samples derived from PPAN (Figures 5a and 5b), the morphology is dominated by elongated, prismatic, and angular crystalline particles with sharper edges. It appears that the porous prill raw material facilitates unconstrained crystal growth during the dissolution-recrystallization cycle. In contrast, in samples derived from TAN (Figures 5c and 5d), the particles are observed to be more agglomerated, forming partially rounded, fused aggregates. While increasing the additive level (from 5.26% to 10%) does not fundamentally alter the primary morphological form, it has been determined that this increase promotes a smoother and more homogeneous distribution of the solid solution phase across the particle surfaces.

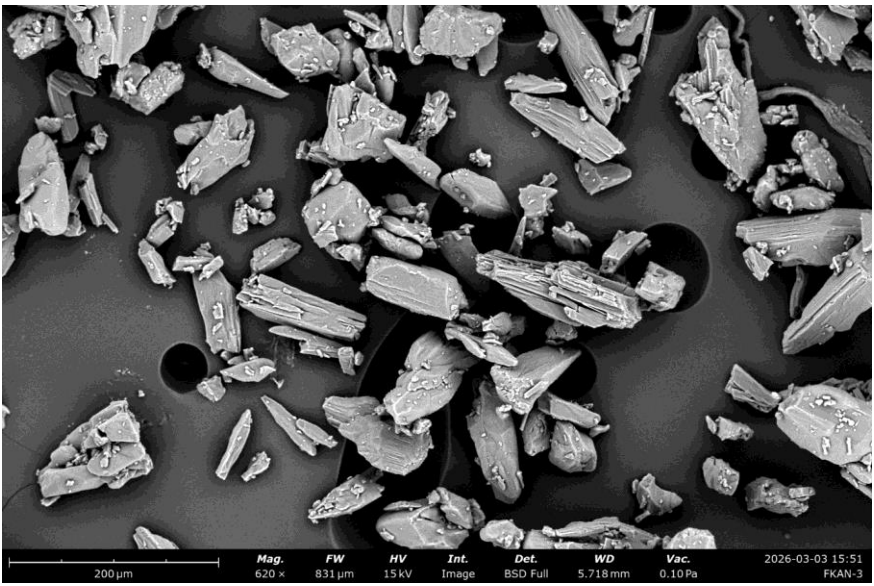
Representative SEM images

Figure 5(a). SEM image of the Experiment 1 / PPAN / 10% sample.



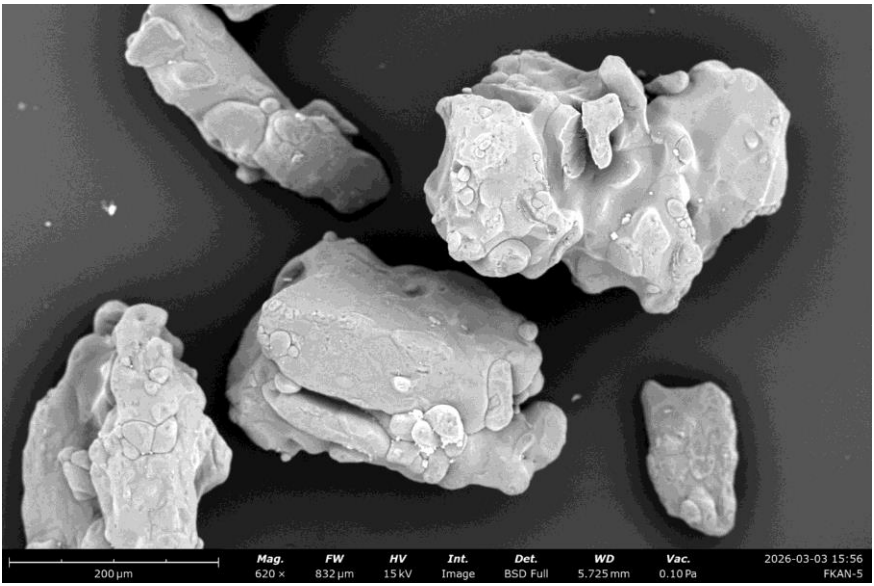
Source: Experimental data from this study.

Figure 5(b). SEM image of the Experiment 3 / PPAN / 5.26% sample.



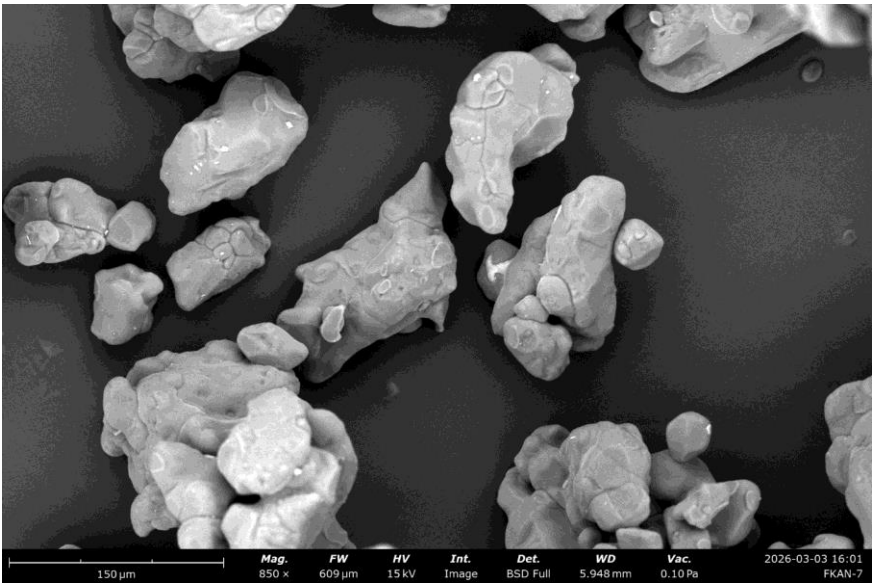
Source: Experimental data from this study.

Figure 5(c). SEM image of the Experiment 5 / TAN / 10% sample.



Source: Experimental data from this study.

Figure 5(d). SEM image of the Experiment 7 / TAN / 5.26% sample.



Source: Experimental data from this study.

Description for Figure 5: Representative SEM images from experiments 1, 3, 5, and 7. The original scale bars, magnifications, and sample labels have been preserved. Morphological assessment was performed qualitatively, taking into account the specific scale bar and magnification for each image.

Evaluation of findings in terms of phase stability

When both additive levels are evaluated together, the composition containing 10% KNO_3 provided more significant stabilization in terms of phase transition behavior. The absence of a distinct DSC peak in the temperature range associated with the IV↔III transition—observed in both PPAN and TAN samples and replicated across two independent preparation trials—supports the stabilizing effect of the KNO_3 additive. Furthermore, differences in the crystalline structure and XRD peaks point to a structural change that is consistent with these thermal findings.

Evaluation from an implementation perspective

The fact that both AN and KNO_3 are chlorine-free components, combined with the observation that the addition of 10% KNO_3 suppresses the phase transition peak near ambient temperature, makes this composition noteworthy for research into AN-based oxidizers with improved phase stability. A comprehensive evaluation of the results from DSC, XRD, TGA, and SEM analyses has clearly demonstrated the favorable phase transition behavior achieved with the 10% KNO_3 additive.

Conclusion

In this study, the effect of KNO_3 addition on the phase transition behavior of TAN and PPAN raw materials was compared. While endothermic transitions were observed in the range of 30.19–38.75 °C for samples containing 5.26% KNO_3, no distinct peaks were identified in the same temperature region for samples containing 10% KNO_3. The fact that this result was obtained for both types of AN and across two independent preparation replicates indicates that the addition of 10% KNO_3 effectively suppresses the thermal event associated with the IV↔III transition.

XRD results revealed the crystalline structure of the samples and the structural variations resulting from the dopant; TGA results indicated the onset of the primary mass loss in the range of 203.85–217.10 °C; and SEM images displayed the characteristic particle morphology of the prepared products. When these findings are evaluated collectively, the addition of 10% KNO_3 emerges as a successful approach for modulating the phase transition behavior of AN near ambient temperature and enhancing its phase stability.

Ethical standards and declarations

Authorship contribution

Ayşen Nur Durgun: Methodology, research, experimental design, data evaluation, visualization, and writing.

Conflict of interest

The author declares that there is no conflict of interest.

Availability of data

The XRD, DSC, TGA, and SEM data evaluated in the study are presented in the relevant tables and figures.

References

Chien, W.-M., Chandra, D., Helmy, A. K., Franklin, J., & Rawn, C. J. (2005). Experimental determination of NH_4NO_3–KNO_3 binary phase diagram. *Journal of Phase Equilibria and Diffusion, 26*, 115–123. https://doi.org/10.1007/s11669-005-0130-4

Coates, R. V., & Crewe, J. M. (1961). Solid solutions in the system ammonium nitrate–potassium nitrate. *Nature, 190*, 1190–1191. https://doi.org/10.1038/1901190a0

Dave, P. N., & Sirach, R. (2023). Comparative study of the thermal decomposition of ammonium nitrate in the presence of nanocrystalline copper ferrite. *Materials Advances, 4*(24), 6665–6672. https://doi.org/10.1039/D3MA00676J

Kaniewski, M., Huculak-Mączka, M., Zieliński, J., Biegun, M., Hoffmann, K., & Hoffmann, J. (2021). Crystalline phase transitions and reactivity of ammonium nitrate in systems containing selected carbonate salts. *Crystals, 11*(10), Article 1250. https://doi.org/10.3390/cryst11101250

Rotariu, T., Pulpea, B.-G., Dîrloman, F.-M., Diacon, A., Rusen, E., Toader, G., Zvîncu, N.-D., Iordache, T.-V., & Botiș, R. H. (2022). The influence of potassium salts phase stabilizers and binder matrix on the properties of novel composite rocket propellants based on ammonium nitrate. *Materials, 15*(24), Article 8960. https://doi.org/10.3390/ma15248960

U.S. Environmental Protection Agency, Occupational Safety and Health Administration, & Bureau of Alcohol, Tobacco, Firearms and Explosives (2015). *Chemical advisory: Safe storage, handling, and management of solid ammonium nitrate prills* (EPA 550-F-15-001). https://nepis.epa.gov/Exe/ZyPURL.cgi?Dockey=P100V369.TXT

Wu, H. B., & Chan, C. K. (2008). Effects of potassium nitrate on the solid phase transitions of ammonium nitrate particles. *Atmospheric Environment, 42*(2), 313–322. https://doi.org/10.1016/j.atmosenv.2007.09.041

BÖLÜM 3

CHARACTERIZATION AND ADSORPTION APPLICATIONS OF ACTIVATED CARBONS ORIGINATING FROM RICE HUSKS

İLKNUR DEMİRAL[1]
CANAN ŞAMDAN[2]
HAKAN DEMİRAL[3]

Introduction

With the growing population, industrialization, and urbanization, water pollution by organic pollutants, synthetic dyes, and heavy metal ions has become a pressing environmental and public health concern. In particular, wastewater from the textile, metal-coating, chemical, pharmaceutical, and petrochemical industries contains toxic and persistent pollutants such as methylene blue, crystal violet, phenolic compounds, and various heavy metal ions (Altıntıg et al., 2015).

[1] Prof. Dr., Eskişehir Osmangazi University, Chemical Engineering, Orcid: 0000-0003-2867-5205
[2] Assoc. Prof. Dr., Eskişehir Osmangazi University, Chemical Engineering, Orcid: 0000-0001-8755-0790
[3] Prof. Dr., Eskişehir Osmangazi University, Chemical Engineering, Orcid: 0000-0003-3038-8598

These compounds, even at low concentrations, can cause ecotoxic effects and pose serious long-term risks to human health. Conventional treatment methods for removing such pollutants are often insufficient and cannot provide a sustainable solution because of high investment and operating costs. In this context, adsorption is considered a prominent method among advanced water treatment technologies, thanks to its high removal efficiency, simple operating conditions, and applicability to a wide range of pollutants (Foroutan et al., 2021). Among the adsorbents used in adsorption processes, activated carbons are considered the most common and effective materials thanks to their high specific surface area, advanced micro- and mesopore structure, and rich surface functional groups. However, the high production costs of commercial activated carbons and their reliance on fossil-based raw materials have accelerated research into producing activated carbon from low-cost, renewable biomass sources in recent years. In this context, agricultural wastes are notable precursor materials due to their abundant availability, low economic value, and carbon-rich lignocellulosic structures (He et al., 2023; Shahrokhi-Shahraki et al., 2021). Beyond dye removal, biomass-derived activated carbons have also been investigated for the adsorption of pharmaceutical pollutants such as amoxicillin (Mustafa Fatih Ergin et al., 2024). Rice is one of the most widely produced crops worldwide, and rice husks have emerged as an important by-product, accounting for approximately 20% of total rice production. The literature reports that hundreds of millions of tons of rice husk waste are released each year globally, and a large share of this waste is disposed of through incineration or landfill. This situation both leads to environmental pollution and causes the loss of an important biomass resource that can be converted into high-value-added products without being evaluated (Cantoni et al., 2021).

Structurally, rice husk differs from many biomass types by containing lignocellulosic components such as cellulose, hemicellulose, and lignin, as well as high levels of amorphous SiO_2. This unique composition enables the production of activated carbons with high porosity when appropriate carbonization and activation strategies are applied. In fact, recent studies have shown that activated carbons produced from rice husks by physical and chemical activation methods exhibit effective performance in water treatment and adsorption applications (He et al., 2023; Jawad et al., 2021). The literature on adsorption applications of rice husk-derived activated carbons shows that they achieve high efficiencies, particularly in removing cationic dyes such as methylene blue and crystal violet. Studies report removal efficiencies above 90%, with adsorption behavior that fits the Langmuir and Freundlich isotherm models (Shen et al., 2022). This high performance is attributed to π-π interactions between aromatic dyestuffs and the carbon surface. Rice husk-based activated carbons have also been reported to remove both organic pollutants and heavy metal ions effectively. In the adsorption of metal ions such as Zn^{2+}, Cr(VI), and Sr^{2+}, surface functional groups (–OH, –COOH, etc.) and pore structure play decisive roles. Adsorption kinetics have been reported to conform mostly to the pseudo-second-order model (Sundriyal et al., 2021).

The activation method and conditions are known to play a decisive role in determining the pore structure and surface chemistry of activated carbons. The literature widely reports that chemical agents such as NaOH, KOH, $ZnCl_2$, and H_3PO_4 produce different pore distributions and surface properties (Y. Huang et al., 2020; Zandifar et al., 2024). Among chemical activation methods, $ZnCl_2$ activation stands out as an effective approach for controlling the pore architecture of rice husk-derived activated carbons. $ZnCl_2$ regulates the loss of volatiles during carbonization by promoting dehydration and aromatic condensation within the lignocellulosic structure,

thereby contributing to the formation of an improved micro-mesopore network. In the literature, $ZnCl_2$-activated rice husk-derived activated carbons have been reported to offer high specific surface areas, with the micro-mesoporous structure dominant (T. Huang et al., 2025; Rahman et al., 2012). Rice husk activated carbons treated with a combination of $ZnCl_2$ and H_3PO_4 also exhibit Type IV nitrogen adsorption isotherms with distinct hysteresis loops, clearly indicating a mesoporous structure. These pore structures are highlighted for strengthening interactions with phenolic compounds and aromatic pollutants (Allwar & Syamsurizal, 2017; Saad et al., 2020). Taken together, these findings show that $ZnCl_2$-activated rice husk-derived activated carbons effectively adsorb a broad range of pollutants, owing to their balanced micro- and mesoporous structure. Therefore, $ZnCl_2$ activation is key to tailoring the structure of rice husk-based activated carbons to the target pollutant in adsorption applications (Abd El-Lateef et al., 2024; Pala et al., 2023). In this study, we characterized the structural and surface properties of rice husk-derived activated carbons and evaluated how different activation strategies affect their adsorption performance.

Material and Method

Raw Material

In this study, agricultural waste rice husks were used as the raw material for activated carbon production. The husks were washed with water and oven-dried to remove dust, soil, and other foreign substances from their surfaces. Before chemical activation, the dried samples were prepared in suitable sizes to ensure homogeneity in the experiments.

Chemical Activation and Carbonization of Rice Husk

The chemical activation method using $ZnCl_2$ was applied in the production of activated carbon from rice husks. A certain amount

of rice husk samples was weighed and impregnated with $ZnCl_2$ at impregnation ratios of 2:1 and 3:1 ($ZnCl_2$: rice husk, by mass). The impregnation process was carried out on a heated magnetic stirrer for 6 hours at 70 °C. After impregnation, the samples were filtered and then dried in an oven. The dried samples were stored in sealed glass containers before carbonization. For carbonization, the $ZnCl_2$-impregnated samples were processed in a vertical tube furnace at temperatures of 400 °C, 500 °C, and 600 °C. During carbonization, nitrogen gas (N_2) was passed through the reactor at a controlled flow rate to provide an inert atmosphere.

After the carbonization process was completed, the samples left to cool in the furnace were removed from the reactor and weighed. The activated carbons obtained were washed first with dilute HCl and then with hot distilled water to remove $ZnCl_2$ and inorganic impurities remaining on the surface. The washing process was continued until the filtrate pH reached 6–7. Finally, the samples were dried in an oven and prepared for characterization and adsorption experiments. The efficiency of activated carbon production was calculated as the ratio of the activated carbon mass obtained after carbonization and washing to the initial mass of the impregnated raw material. Yield values were determined using the post-washing masses of activated carbons obtained at different impregnation ratios (2:1 and 3:1) and different carbonization temperatures.

Characterization of Activated Carbons

BET surface area analysis was conducted to determine the structural properties of activated carbons produced through chemical activation and carbonization. The specific surface area (S_{BET}), micropore volume, total pore volume, and mean pore diameter of the activated carbons were determined by BET analysis. Scanning Electron Microscopy (SEM) analyses were performed to examine

the surface morphology and pore structure of the samples. SEM and EDS analyses were conducted using the Hitachi Regulus 8230 FE-SEM device; the surface structures of the raw materials and selected activated carbon samples were evaluated comparatively.

Methylene Blue Adsorption Tests

The methylene blue (MB) adsorption capacities of activated carbons prepared at a $ZnCl_2$-rice husk impregnation ratio of 3:1 and at carbonization temperatures of 400, 500, and 600 °C were determined at initial concentrations of 100, 200, and 300 mg L^{-1}. The effect of the adsorbent dose of the PK3:1/500 sample on adsorption performance was investigated by batch experiments conducted with 0.05 L of 100 mg L^{-1} MB solution at pH 6 and 25 °C for 24 hours. The effect of contact time was evaluated using 0.15 g of PK3:1/500 and a 100 mg L^{-1} MB solution at 25 °C. The effect of initial dye concentration was investigated by contacting 0.15 g of PK3:1/500 with MB solutions of different initial concentrations at 25 °C for 5 h. After adsorption, the activated carbon particles were separated from the solution, and the residual MB concentration in the supernatant was determined using UV–Vis spectrophotometry. The amount of substance adsorbed per unit mass of adsorbent (q_t, mg g^{-1}) was calculated using Eq. (1), and the percent adsorption efficiency was calculated using Eq. (2):

$$q_t = \frac{(C_0 - C_e).V}{m} \qquad Eq.1.$$

$$\%\ Adsorption = \frac{(C_0 - C_e)}{C_0} * 100 \qquad Eq.2$$

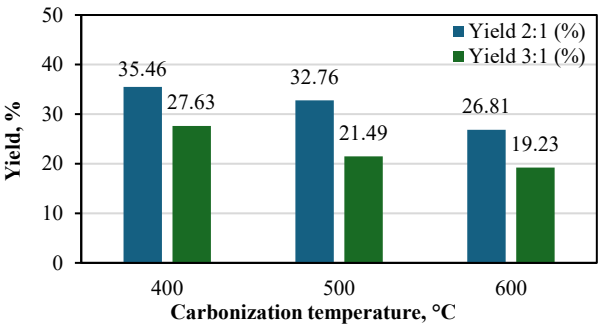
Where: q_t: adsorption capacity (mg g^{-1}); C_0: initial concentration (mg L^{-1}); Ce: concentration after adsorption (mg L^{-1}); V: solution volume (L); m: mass of adsorbent (g).

Results and discussion

The Effect of Carbonization Temperature and $ZnCl_2$ Ratio on Activated Carbon Yield

Figure 1 shows the yields of activated carbons produced from rice husk at different $ZnCl_2$ impregnation ratios and carbonization temperatures. The yield of $ZnCl_2$-activated rice husk-based activated carbon decreases as the carbonization temperature rises. For both impregnation ratios, the yield is highest at 400 °C and drops markedly at 600 °C. At every temperature, the 2:1 $ZnCl_2$ impregnation ratio produces a higher yield than the 3:1 ratio. This may be due to increased degradation and gasification losses, as well as further decomposition of volatile components and the carbon matrix at higher carbonization temperatures. Previous studies have reported that carbon loss increases at high temperatures following $ZnCl_2$ activation, resulting in a lower yield. (Maniarasu et al., 2023; Menya et al., 2018). These data show that a carbonization temperature of 400 °C and a 2:1 $ZnCl_2$ impregnation ratio provide more favorable conditions for activated carbon yield.

Figure 1. Effect of $ZnCl_2$ impregnation rate and carbonization temperature on activated carbon yield.



Source: This study.

Impact of Carbonization Temperature and Chemical Activation on Structural Properties

The carbonization temperature and chemical activation conditions play a decisive role in shaping the pore structure of rice husk-based activated carbons. $ZnCl_2$ activation promotes pore formation by facilitating dehydration and aromatic condensation in the biomass during carbonization. These reactions preserve the carbon skeleton while contributing to porosity. Studies have also found that $ZnCl_2$ drives the thermal degradation of lignocellulosic structures, particularly at moderate temperatures (400–600 °C), encouraging the carbon matrix to develop a porous structure rather than collapse (Chen et al., 2016).

Table 1. BET analysis results

	S_{BET} (m^2 g^{-1})	V_{MIC} (cm^3g^{-1})	V_{MES} (cm^3g^{-1})	V_{TOT} (cm^3 g^{-1})	D_p (Å)
PK2:1/400	293.2	0.122	0.22	0.342	46.77
PK2:1/500	782.95	0.299	0.14	0.439	22.44
PK2:1/600	763.20	0.293	0.169	0.462	24.64
PK3:1/400	978.75	0.484	0.075	0.559	22.88
PK3:1/500	1524.35	0.570	0.257	0.827	21.72
PK3:1/600	1221.72	0.438	0.256	0.694	22.75

Source: This study.

The BET analysis in Table 1 shows that carbonization temperature and $ZnCl_2$ impregnation ratio influence the surface area and pore structure of rice husk-derived activated carbons. Increasing the temperature from 400 to 500 °C raised the specific surface area and micropore volume at both impregnation ratios. At a 2:1 ratio, the specific surface area rose from 293.2 to 782.95 m^2 g^{-1}; at a 3:1 ratio, it increased from 978.75 to 1524.35 m^2 g^{-1}. Increasing the impregnation ratio from 2:1 to 3:1 also increased specific surface area, micropore volume, and total pore volume at all temperatures. Mesopore volume, however, showed a different trend: at 400 °C, it fell from 0.220 to 0.075 cm^3 g^{-1} as the impregnation ratio increased.

Raising the carbonization temperature from 500 to 600 °C reduced the specific surface area and micropore volume at both impregnation ratios. At a 2:1 ratio, mesopore volume increased from 0.140 to 0.169 $cm^3\ g^{-1}$, while total pore volume rose from 0.439 to 0.462 $cm^3\ g^{-1}$, suggesting a shift toward wider pores. At a 3:1 ratio, mesopore volume remained nearly constant, while total pore volume decreased from 0.827 to 0.694 $cm^3\ g^{-1}$. Mean pore diameter increased slightly at both ratios over this temperature range. Of the conditions investigated, an impregnation ratio of 3:1 and a carbonization temperature of 500 °C yielded the highest specific surface area (1524.35 $m^2\ g^{-1}$), micropore volume (0.570 $cm^3\ g^{-1}$), and total pore volume (0.827 $cm^3\ g^{-1}$).

Adsorption – Desorption Isotherm Results

Figures 2 and 3 show the adsorption-desorption isotherms of activated carbons prepared using $ZnCl_2$ at impregnation ratios of 2:1 and 3:1 and at different carbonization temperatures. The sharp increase in N_2 adsorption at low relative pressures ($P/P_0 < 0.1$) indicates micropore filling, while adsorption at higher relative pressures reflects contributions from wider pores. The gradual increase in adsorption at medium and high relative pressures ($P/P_0 > 0.4$), together with the hysteresis loop in samples synthesized at 400 °C, indicates that the isotherms also exhibit Type IV character. This suggests the development of a micropore-mesopore combination alongside H4-like hysteresis (Lin et al., 2013; Wazir et al., 2020). At a 3:1 $ZnCl_2$ impregnation ratio, samples carbonized at 500 and 600 °C showed higher adsorption volumes than those prepared at a 2:1 ratio. The sample carbonized at 500 °C had the highest adsorption capacity, both in micropore filling and mesopore contribution. This behavior suggests that carbonization temperature and $ZnCl_2$ loading jointly control the pore structure (Allwar & Syamsurizal, 2017).

Figure 2. N_2 adsorption–desorption isotherms of activated carbons at an impregnation ratio of 2:1 $ZnCl_2$.

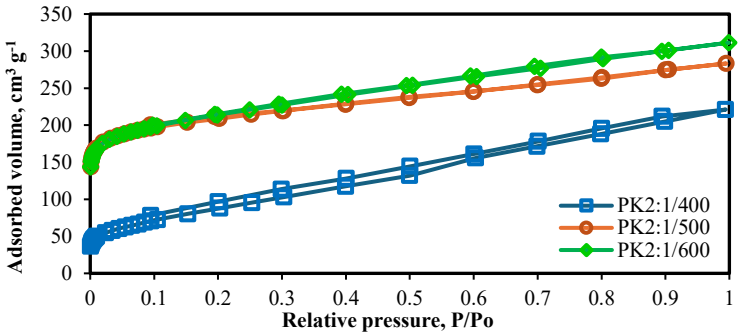
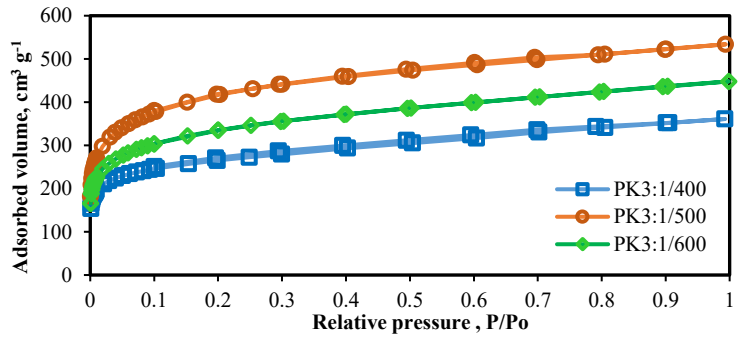


Figure 3. N_2 adsorption–desorption isotherms of activated carbons at an impregnation ratio of 3:1 $ZnCl_2$.

Source: This study.



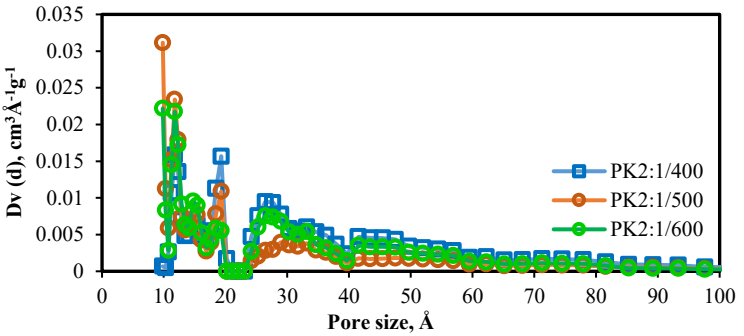
Source: This study.

Pore Size Distributions

The pore size distributions of activated carbons synthesized with $ZnCl_2$ at impregnation ratios of 2:1 and 3:1 and at different carbonization temperatures are shown in Figures 4 and 5. The pore size distributions indicate the presence of micropores (<20 Å), consistent with micropore formation during $ZnCl_2$ activation. At a 2:1 $ZnCl_2$ impregnation ratio, pore distribution appears to broaden as the carbonization temperature increases. The sample produced at 400 °C had a higher mesopore volume than micropore volume,

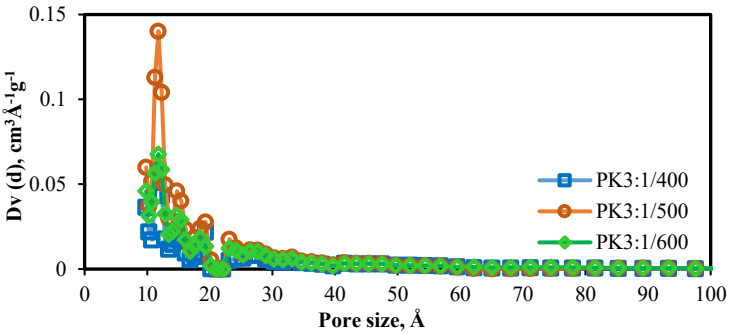
whereas micropores were dominant at 500 and 600 °C. At a 3:1 ratio, higher pore volumes were observed in the micropore region, particularly at 500 °C, indicating that the increased $ZnCl_2$ amount promoted micropore formation.

Figure 4. Pore size distribution for all temperatures at a 2:1 impregnation ratio



Source: This study.

Figure 5. Pore size distribution at 3:1 impregnation ratio and at all temperatures

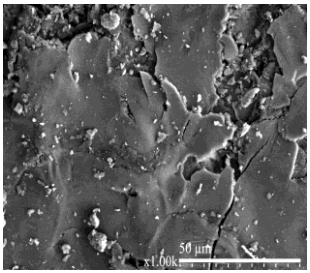


Source: This study.

SEM and EDS Analysis

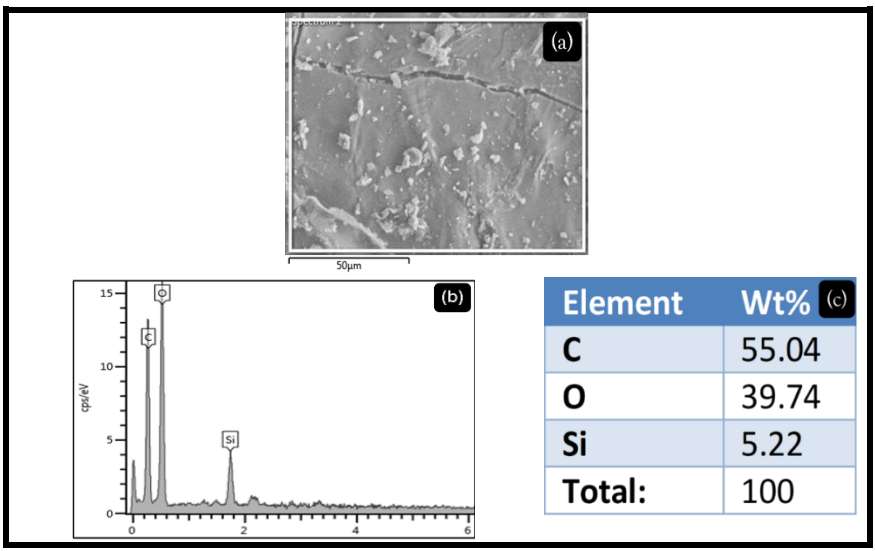
Scanning electron microscopy (SEM) is a valuable characterization technique for closely examining materials' surface morphology, pore structure, and surface-dependent physical properties.

Figure 6. SEM image of the raw material



Source: This study.

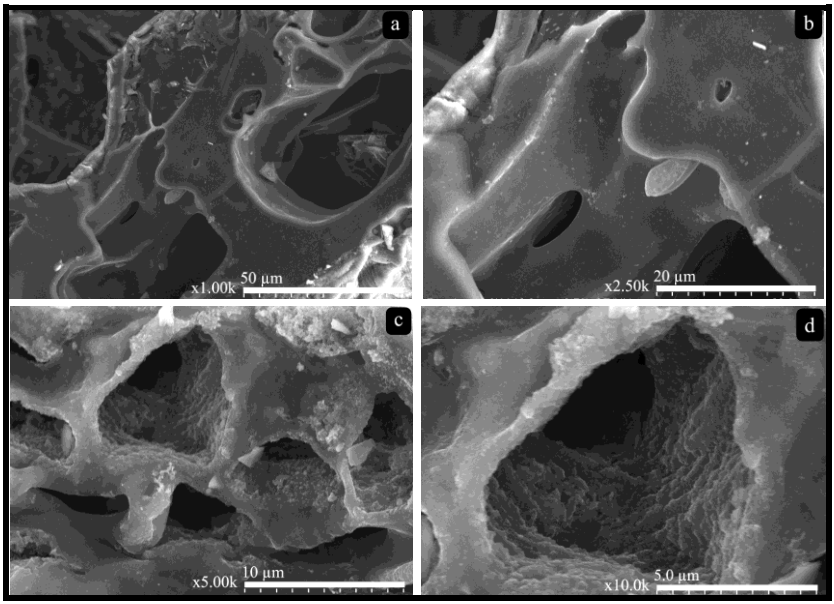
Figure 7. EDS analysis results of the raw material



Source: This study.

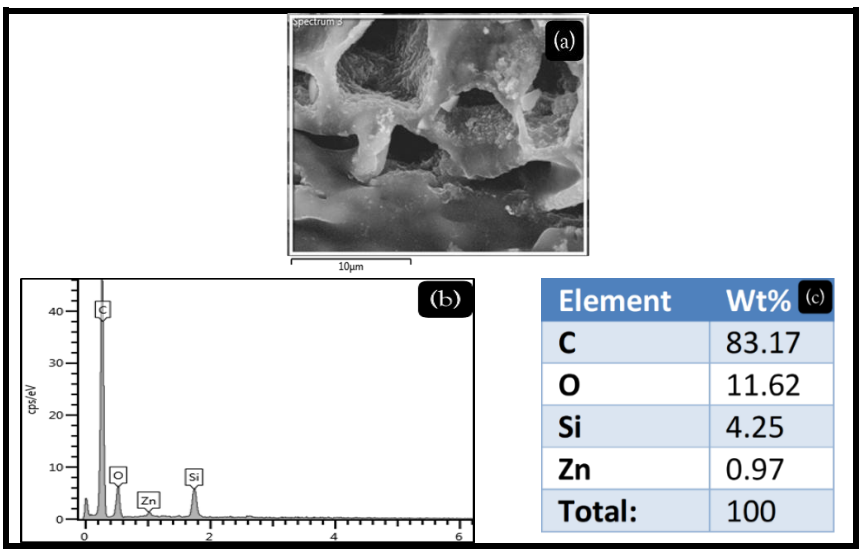
In this study, SEM analysis was used to compare the morphological properties of activated carbon produced from rice husk through $ZnCl_2$ activation, followed by carbonization at 500 °C, using a 3:1 impregnation ratio. SEM images of rice husk and PK3:1/500 samples are shown in Figures 6 and 8, respectively. The EDS spectra of the raw material and PK3:1/500 are presented in Figures 7 and 9, respectively.

Figure 8. SEM images of PK3:1/500 : (a) x1000, (b) x2500, (c) x5000, (d) x10000



Source: This study.

Figure 9. EDS analysis results of PK3:1/500



Element	Wt%
C	83.17
O	11.62
Si	4.25
Zn	0.97
Total:	100

Source: This study.

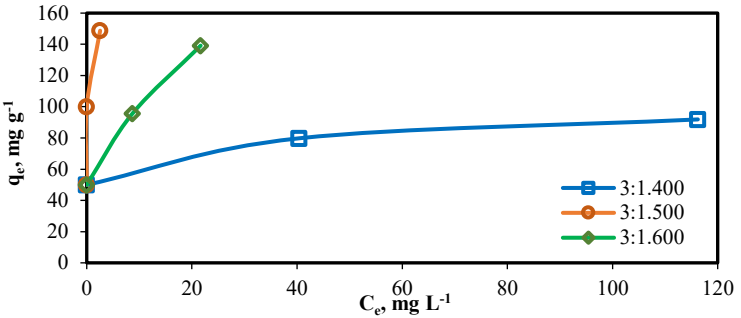
Methylene Blue adsorption results

This section examines methylene blue adsorption by rice husk-derived activated carbons and the effect of surface area, considering key parameters such as adsorbent amount, contact time, and initial concentration. The experimental data are analyzed using adsorption kinetics and isotherm models to provide a holistic understanding of the adsorption mechanism and interactions between the activated carbon and dye.

Effect of surface area on adsorption

In Figure 10, the methylene blue (MB) adsorption behavior of activated carbons synthesized at a 3:1 impregnation ratio and activation temperatures of 400, 500, and 600 °C was evaluated using initial concentrations of 100, 200, and 300 mg L^{-1}. Adsorption capacities are plotted against the equilibrium concentration (C_e). The increase in adsorption capacity (q_e) with increasing C_e across all samples may be attributed to the higher dye concentration in solution, the stronger mass-transfer driving force between the adsorbent and adsorbate, and more effective use of the active surface regions. This trend has been widely reported in numerous studies of dye adsorption on activated carbons (Mohan & Pittman Jr., 2006; Rafatullah et al., 2010). The lower q_e values of activated carbon produced at 400 °C may be attributed to limited pore development, resulting in a lower surface area and accessible pore volume (Gayathiri et al., 2022). On the other hand, a significant increase in adsorption capacity was observed in activated carbons treated at 500 °C, and especially at 600 °C. Comprehensive reviews of biomass-based activated carbons identify the key factors governing adsorption performance: specific surface area, micro- and mesopore distribution, and surface chemistry (Pellenz et al., 2023).

Figure 10. Adsorption capacities of activated carbons produced at 400, 500, and 600 °C at a 3:1 impregnation ratio

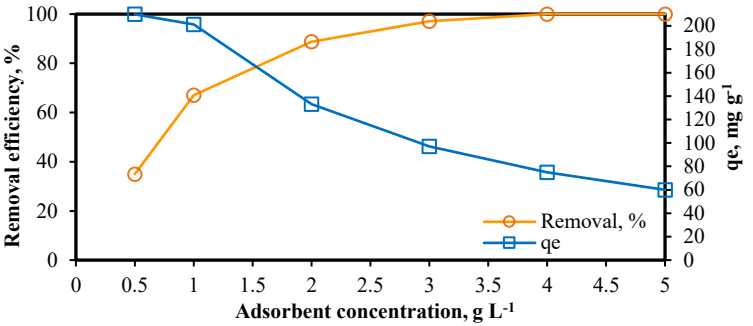


Source: This study.

Effect of Activated Carbon Amount on Adsorption

Figure 11 shows the removal efficiency (%) and equilibrium adsorption capacity (q_e) at different adsorbent doses. As the amount of activated carbon increased, methylene blue removal rose significantly, exceeding 95% at adsorbent amounts of 0.15 g (3 g L^{-1}) and above. This trend may be explained by the increased availability of active adsorption sites for dye molecules in the solution (Shafeeyan et al., 2010). On the other hand, increasing the activated carbon dose decreased the q_e values, which represent the amount of dyestuff adsorbed per unit mass of adsorbent. This may be because, although higher adsorbent doses provide a greater total adsorption surface, the amount of available dyestuff is limited relative to the adsorbent mass. These results indicate that the increase in removal efficiency and the decrease in adsorption capacity per unit mass (q_e) with increasing adsorbent dose are consistent with findings from similar studies in the literature. Accordingly, an adsorbent dose of approximately 3 g L^{-1} for PK3:1/500 can be considered optimal for methylene blue removal, achieving a removal efficiency of over 95% while limiting the decrease in adsorption capacity.

Figure 11. Effect of PK3:1/500 amount on methylene blue adsorption yield and adsorption capacity (q_e)

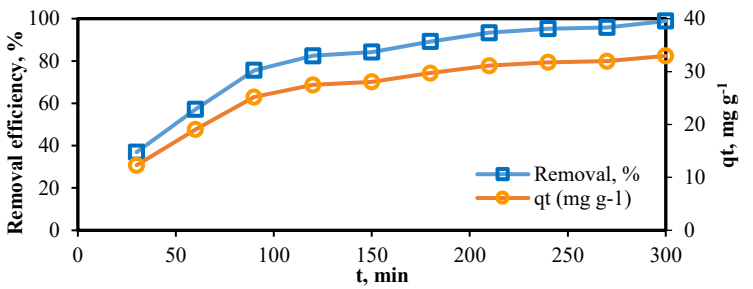


Source: This study.

The Effect of Contact Time on Adsorption

To assess the effect of contact time on methylene blue adsorption, experiments were conducted at 25 °C using a 100 mg L^{-1} methylene blue solution and 0.15 g of PK3:1/500. Figure 12 shows the removal percentage and adsorption capacity (q_t) measured over time.

Figure 12. Effect of contact time on removal efficiency and qt in methylene blue adsorption with PK3:1/500

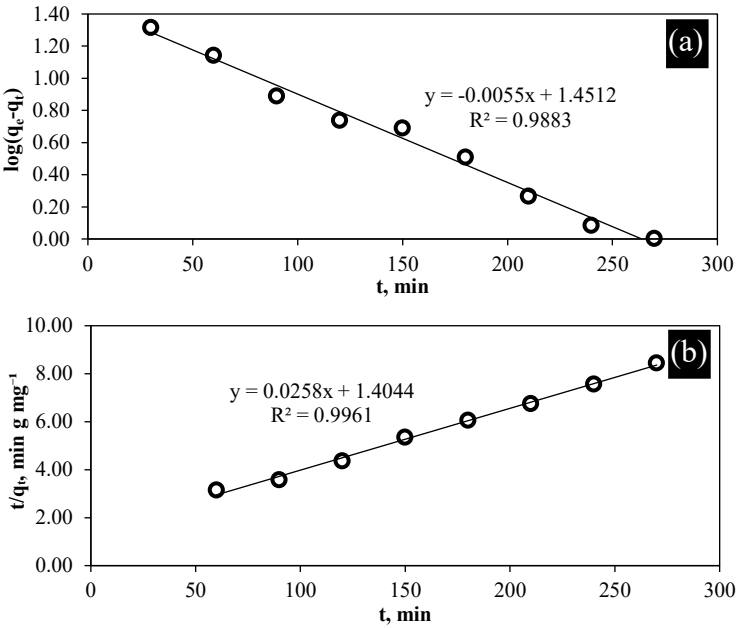


Source: This study.

As shown in Figure 12, methylene blue adsorption increased rapidly over the first 90 min, reaching approximately 75%. This initial rapid uptake may be due to the abundance of readily accessible

adsorption sites on the PK3:1/500 surface. After 90 min, the adsorption rate gradually declined as MB molecules occupied the available active sites and the concentration gradient at the adsorbent surface decreased. Only minor changes were observed after about 240 min, indicating that the adsorption system was approaching equilibrium. Figure 13 compares the fit of the methylene blue adsorption kinetic data for PK3:1/500 to the pseudo-first-order and pseudo-second-order kinetic models.

Figure 13. Effect of contact time on methylene blue adsorption with PK3:1/500: (a) pseudo-first-order kinetic model and (b) pseudo-second-order kinetic model.



Source: This study.

The pseudo-first-order model has a correlation coefficient of 0.9883 and a rate constant (k_1) of 0.0127 min^{-1}. By comparison, the pseudo-second-order model has a higher correlation coefficient of 0.9961 and a rate constant (k_2) of 4.74×10^{-4} g mg^{-1} min^{-1}, indicating a better fit to the experimental kinetic data. Therefore, the pseudo-

second-order kinetic model provided a better fit to the experimental data.

Adsorption isotherms

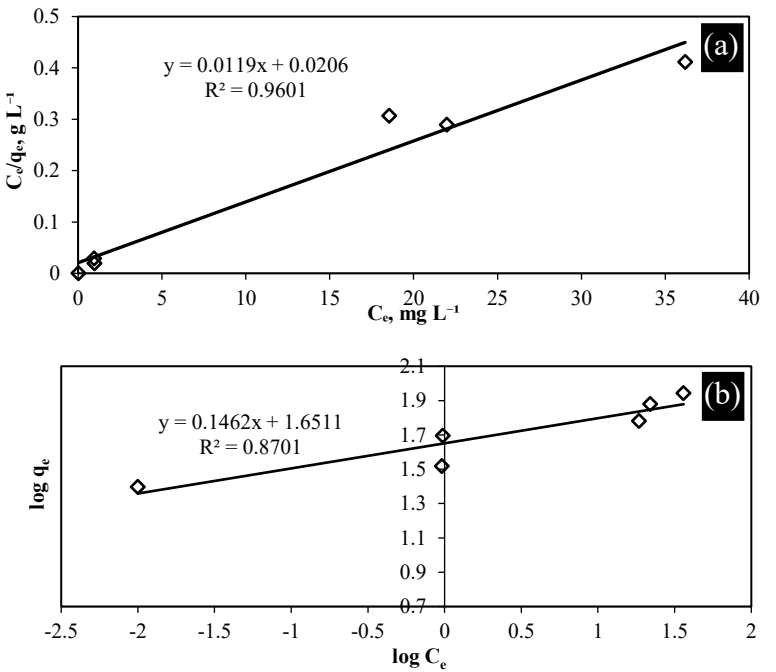
To examine the effect of initial concentration on adsorption, 0.15 g of activated carbon was added to methylene blue solutions with varying initial concentrations and kept at 25 °C for 5 hours.

Table 2. Langmuir and Freundlich isotherm constants

Parameters	Value	Parameters	Value
q_{max}	84.03 mg g^{-1}	K_F	44.79
K_L	0.578 L mg^{-1}	n	6.84
R^2	0.96	R^2	0.87

Source: This study.

Figure 14. Effect of initial concentration on methylene blue adsorption by PK3:1/500: (a) Langmuir isotherm and (b) Freundlich isotherm



Source: This study.

After adsorption, the remaining methylene blue concentrations were measured, and the resulting data were used to determine the equilibrium adsorption behavior using the Langmuir and Freundlich isotherms. The concentration-dependent adsorption behavior is shown in Figure 14, and the calculated isotherm model constants are listed in Table 2. The Langmuir model provided a better fit (R^2 = 0.96) than the Freundlich model (R^2 = 0.87), with an estimated maximum adsorption capacity of 84.03 mg g^{-1}.

Discussion of results and recommendations

In this study, activated carbons were produced from rice husks using $ZnCl_2$ chemical activation. The effects of carbonization temperature and impregnation ratio on yield, pore structure, and methylene blue adsorption were examined. Yield decreased as carbonization temperature and $ZnCl_2$ impregnation ratio increased. The highest efficiency was achieved with a 2:1 impregnation ratio, yielding 35.46% at 400 °C. The most suitable production conditions for surface area and pore properties were a $ZnCl_2$/rice husk impregnation ratio of 3:1 and a carbonization temperature of 500 °C. Under these conditions, the PK3:1/500 sample had a specific surface area of 1524.35 m^2 g^{-1}, a micropore volume of 0.570 cm^3 g^{-1}, and a total pore volume of 0.827 cm^3 g^{-1}. Most samples had a higher micropore volume than mesopore volume, except for PK2:1/400. PK3:1/500 exhibited the highest BET surface area and was selected for further adsorption experiments. At adsorbent concentrations of 3 g L^{-1} and above, removal efficiency exceeded 95%, and adsorption equilibrium was reached after approximately 240 minutes. The kinetic data fit the pseudo-second-order model better (R^2 = 0.9961), although both kinetic models showed high correlation coefficients. The equilibrium data fit the Langmuir model better than the Freundlich model (R^2 = 0.9601). Overall, the results indicate that rice husk can be converted into activated carbon with a high surface area and improved pore structure under suitable activation conditions.

The PK3:1/500 sample was found to be an effective adsorbent for methylene blue removal, demonstrating the potential to convert rice husk into an environmentally friendly, value-added product.

Acknowledgments

We would like to thank the students in the 2023-2024 and 2024-2025 Engineering Research courses for their contributions.

References

Abd El-Lateef, H. M., Zeng, C.-Q., Khalaf, M. M., & Mohamed, I. M. A. (2024). Green Synthesis of Silver-Incorporated Rutile TiO2 for Enhanced Photocatalytic Degradation of Ciprofloxacin and Carmine G Dye Pollutants. *Catalysts*, *14*(12), 904. https://doi.org/10.3390/catal14120904

Allwar, A., & Syamsurizal, S. (2017). Removal of 2-chlorophenol Using Rice Husk Activated Carbon Prepared by zncl2/h3po4 Activation. *Oriental Journal of Chemistry*, *33*(5), 2386–2393. https://doi.org/10.13005/ojc/330531

Altıntıg, E., Acar, I., Altundag, H., & Ozyıldırım, O. (2015). Production Of Activated Carbon From Rice Husk To Support Zn2+ Ions. *Fresenius Environmental Bulletin*, (4).

Cantoni, B., Turolla, A., Wellmitz, J., Ruhl, A. S., & Antonelli, M. (2021). Perfluoroalkyl substances (PFAS) adsorption in drinking water by granular activated carbon: Influence of activated carbon and PFAS characteristics. *Science of The Total Environment*, *795*, 148821. https://doi.org/10.1016/j.scitotenv.2021.148821

Chen, X., Fang, Y., Zhu, J., Wang, F., Zhao, T., & Fan, D. (2016). *Preparation and Properties of Rice Husk-based Activated Carbon Using Phosphoric Acid as Activator:* International Conference on Electronics, Mechanics, Culture and Medicine, Shenyang, China. https://doi.org/10.2991/emcm-15.2016.68

Foroutan, R., Peighambardoust, S. J., Peighambardoust, S. H., Pateiro, M., & Lorenzo, J. M. (2021). Adsorption of Crystal Violet Dye Using Activated Carbon of Lemon Wood and Activated Carbon/Fe3O4 Magnetic Nanocomposite from Aqueous Solutions: A Kinetic, Equilibrium and

Thermodynamic Study. *Molecules*, *26*(8), 2241. https://doi.org/10.3390/molecules26082241

Gayathiri, M., Pulingam, T., Lee, K. T., & Sudesh, K. (2022). Activated carbon from biomass waste precursors: Factors affecting production and adsorption mechanism. *Chemosphere*, *294*, 133764. https://doi.org/10.1016/j.chemosphere.2022.133764

He, S., Ling, L., Wu, Y., Yang, S., Hua, Z., Tang, K., Wang, M., Zhu, M., & Fang, J. (2023). Roles of Activated Carbon in UV/Chlorine/Activated Carbon–TiO_2 Process for Micropollutant Abatement and DBP Control. *Environmental Science & Technology*, *57*(24), 9055–9063. https://doi.org/10.1021/acs.est.3c01989

Huang, T., Dong, X., Huang, W., Song, J., Zheng, Q., Li, Z., Han, Y., Xie, E., Wang, S., Yang, Y., & Tan, Z. (2025). Construction of activated carbon/activated carbon fibre capacitive deionization composite electrode and its potential

application in desalination of brackish water. *Desalination*, *593*, 118191. https://doi.org/10.1016/j.desal.2024.118191

Huang, Y., Liu, Y., Wang, W., Chen, M., Li, H., Lee, S., Ho, W., Huang, T., & Cao, J. (2020). Oxygen vacancy–engineered δ-MnO /activated carbon for room-temperature catalytic oxidation of formaldehyde. *Applied Catalysis B: Environmental*, *278*, 119294. https://doi.org/10.1016/j.apcatb.2020.119294

Jawad, A. H., Saud Abdulhameed, A., Wilson, L. D., Syed-Hassan, S. S. A., ALOthman, Z. A., & Rizwan Khan, M. (2021). High surface area and mesoporous activated carbon from KOH-activated dragon fruit peels for methylene blue dye adsorption: Optimization and mechanism study. *Chinese Journal of Chemical Engineering*, *32*, 281–290. https://doi.org/10.1016/j.cjche.2020.09.070

Lin, L., Zhai, S.-R., Xiao, Z.-Y., Song, Y., An, Q.-D., & Song, X.-W. (2013). Dye adsorption of mesoporous activated carbons produced from NaOH-pretreated rice husks. *Bioresource*

Technology, *136*, 437–443. https://doi.org/10.1016/j.biortech.2013.03.048

Maniarasu, R., Rathore, S. K., & Murugan, S. (2023). Biomass-based activated carbon for CO_2 adsorption–A review. *Energy & Environment*, *34*(5), 1674–1721. https://doi.org/10.1177/0958305X221093465

Menya, E., Olupot, P. W., Storz, H., Lubwama, M., & Kiros, Y. (2018). Production and performance of activated carbon from rice husks for removal of natural organic matter from water: A review. *Chemical Engineering Research and Design*, *129*, 271–296. https://doi.org/10.1016/j.cherd.2017.11.008

Mohan, D., & Pittman Jr., C. U. (2006). Activated carbons and low cost adsorbents for remediation of tri- and hexavalent chromium from water. *Journal of Hazardous Materials*, *137*(2), 762–811. https://doi.org/10.1016/j.jhazmat.2006.06.060

Mustafa Fatih Ergin, Hülya Çelik Onar, & Hasniye Yaşa. (2024). Newly adsorbents used to remove amoxicillin from wastewater. In *New Studies in Engineering* (pp. 32–46). Duvar Yayınları.

Pala, J., Le, T., Kasula, M., & Rabbani Esfahani, M. (2023). Systematic investigation of PFOS adsorption from water by Metal Organic Frameworks, Activated Carbon, Metal Organic Framework@Activated Carbon, and functionalized Metal Organic Frameworks. *Separation and Purification Technology*, *309*, 123025. https://doi.org/10.1016/j.seppur.2022.123025

Pellenz, L., De Oliveira, C. R. S., Da Silva Júnior, A. H., Da Silva, L. J. S., Da Silva, L., Ulson De Souza, A. A., De Souza, S. M. D. A. G. U., Borba, F. H., & Da Silva, A. (2023). A comprehensive guide for characterization of adsorbent materials. *Separation and Purification Technology*, *305*, 122435. https://doi.org/10.1016/j.seppur.2022.122435

Rafatullah, Mohd., Sulaiman, O., Hashim, R., & Ahmad, A. (2010). Adsorption of methylene blue on low-cost adsorbents: A review. *Journal of Hazardous Materials*, *177*(1–3), 70–80. https://doi.org/10.1016/j.jhazmat.2009.12.047

Rahman, M. A., Amin, S. M. R., & Alam, A. M. S. (2012). Removal of Methylene Blue from Waste Water Using Activated Carbon Prepared from Rice Husk. *Dhaka University Journal of Science*, *60*(2), 185–189. https://doi.org/10.3329/dujs.v60i2.11491

Saad, M. J., Chia, C. H., Misran, S., Zakaria, S., Sajab, M. S., & Abdul Rahman, M. H. (2020). Rice Husk Activated Carbon with NaOH Activation: Physical and Chemical Properties. *Sains Malaysiana*, *49*(09), 2261–2267. https://doi.org/10.17576/jsm-2020-4909-23

Shafeeyan, M. S., Daud, W. M. A. W., Houshmand, A., & Shamiri, A. (2010). A review on surface modification of activated carbon for carbon dioxide adsorption. *Journal of Analytical*

and Applied Pyrolysis, *89*(2), 143–151. https://doi.org/10.1016/j.jaap.2010.07.006

Shahrokhi-Shahraki, R., Benally, C., El-Din, M. G., & Park, J. (2021). High efficiency removal of heavy metals using tire-derived activated carbon vs commercial activated carbon: Insights into the adsorption mechanisms. *Chemosphere*, *264*, 128455. https://doi.org/10.1016/j.chemosphere.2020.128455

Shen, Z., Xing, X., Wang, S., Lv, M., Li, J., & Li, T. (2022). Effect of K-Modified Blue Coke-Based Activated Carbon on Low Temperature Catalytic Performance of Supported Mn–Ce/Activated Carbon. *ACS Omega*, *7*(10), 8798–8807. https://doi.org/10.1021/acsomega.1c07076

Sundriyal, S., Shrivastav, V., Pham, H. D., Mishra, S., Deep, A., & Dubal, D. P. (2021). Advances in bio-waste derived activated carbon for supercapacitors: Trends, challenges and prospective. *Resources, Conservation and Recycling*, *169*, 105548. https://doi.org/10.1016/j.resconrec.2021.105548

Wang, L., Zhao, M., Ma, H., Han, G., Yang, D., Chen, D., Zhang, Y., & Zhou, J. (2020). Extraction of SiO2 from gasified rice husk carbon simultaneously rice husk activated carbon production: Restudy on product properties, activation mechanism, and evolution law of pore structure. *Energy Reports*, *6*, 3094–3103. https://doi.org/10.1016/j.egyr.2020.11.031

Wazir, A. H., Wazir, I. U., & Wazir, A. M. (2020). Preparation and characterization of rice husk based physical activated carbon. *Energy Sources, Part A: Recovery, Utilization, and Environmental Effects*, 1–11. https://doi.org/10.1080/15567036.2020.1715512

Zandifar, A., Esmaeilzadeh, F., & Rodríguez-Mirasol, J. (2024). Hydrogen-rich gas production via supercritical water gasification (SCWG) of oily sludge over waste tire-derived activated carbon impregnated with Ni: Characterization and optimization of activated carbon production. *Environmental*

Pollution, *342*, 123078. https://doi.org/10.1016/j.envpol.2023.123078


BİDGE